The Astrophysical Journal, 976:205 (18pp), 2024 December 1 https://doi.org/10.3847/1538-4357/ad8238

DIISC-IV. DIISCovery of Anomalously Low Metallicity H II Regions in NGC 99: Indirect Evidence of Gas Inflows

Alejandro J. Olvera[1], Sanchayeeta Borthakur[1], Mansi Padave[1], Timothy Heckman[1,2], Hansung B. Gim[1,3], Brad Koplitz[1], Christopher Dupuis[1], Emmanuel Momjian[4], and Rolf A. Jansen[1]

[1] School of Earth and Space Exploration, Arizona State University, 781 Terrace Mall, Tempe, AZ 85287, USA; ajolver2@asu.edu
[2] Department of Physics & Astronomy, Johns Hopkins University, Baltimore, MD 21218, USA
[3] Department of Physics, Montana State University, P.O. Box 173840, Bozeman, MT 59717, USA
[4] National Radio Astronomy Observatory, 1003 Lopezville Road, Socorro, NM 87801, USA

Received 2024 March 28; revised 2024 July 24; accepted 2024 August 11; published 2024 November 25

Abstract

As a part of the Deciphering the Interplay between the Interstellar medium, Stars, and the Circumgalactic medium (DIISC) survey, we investigate indirect evidence of gas inflow into the disk of the galaxy NGC 99. We combine optical spectra from the Binospec spectrograph on the MMT telescope with optical imaging data from the Vatican Advanced Technology Telescope, radio H I 21 cm emission images from the NSF Karl G. Jansky's Very Large Array, and UV spectroscopy from the Cosmic Origins Spectrograph on the Hubble Space Telescope. We measure emission lines (Hα, Hβ, [O III]λ5007, [N II]λ6583, and [S II]λ6717, 31) in 26 H II regions scattered about the galaxy and estimate a radial metallicity gradient of -0.017 dex kpc^{-1} using the N2 metallicity indicator. Two regions in the sample exhibit an anomalously low metallicity (ALM) of $12 + \log(\mathrm{O/H}) = 8.36$ dex, which is $\sim$0.16 dex lower than other regions at that galactocentric radius. They also show a high difference between their H I and Hα line of sight velocities on the order of 35 km s^{-1}. Chemical evolution modeling indicates gas accretion as the cause of the ALM regions. We find evidence for corotation between the interstellar medium of NGC 99 and Lyα clouds in its circumgalactic medium, which suggests a possible pathway for low metallicity gas accretion. We also calculate the resolved Fundamental Metallicity Relation (rFMR) on subkiloparsec scales using localized gas-phase metallicity, stellar mass surface density, and star formation rate surface density. The rFMR shows a similar trend as that found by previous localized and global FMR relations.

Unified Astronomy Thesaurus concepts: Circumgalactic medium (1879); Galaxy abundances (574); Galaxy accretion (575); Galaxy chemical evolution (580); H II regions (694)

Materials only available in the online version of record: animation

1. Introduction

Cosmological simulations confirm that gas cycling in and out of galaxies, also known as the baryon cycle, is crucial to their growth. Gas inflows into galactic disks are necessary to maintain star formation over cosmic time, whereas galactic outflows are important to regulating star formation rates (D. Kereš et al. 2005; P. F. Hopkins et al. 2014; C.-A. Faucher-Giguère & S. P. Oh 2023). The interstellar medium (ISM) serves as the center stage for the baryon cycle as it is where accreted gas may collapse to form stars and where outflows from stellar remnants are produced. Thus, in order to further understand the physical mechanisms affecting the ISM, it is vital to know its atomic gas content (M_{HI}), molecular gas content ($M_{\mathrm{H_2}}$), star formation rate (SFR), and metallicity (Z).

Measurement of metal abundances in galaxies provides an observational approach to inferring gas in/outflows and star formation since most metals are the result of the nucleosynthesis within stars and in their supernovae explosions (K. Finlator & R. Dave 2008; S. J. Lilly et al. 2013; F. Belfiore et al. 2016). Therefore, the radial metallicity gradient of galaxies is of great interest to study how galaxies grow (e.g., inside-out or outside-in; G. Pezzulli & F. Fraternali 2016; R. B. Larson 1976; F. Matteucci & P. Francois 1989; A. Acharyya et al. 2020; E. Wang & S. J. Lilly 2022). In the local Universe, most massive galaxies show a negative metallicity gradient with metallicity dropping with galactocentric radius (M. B. Vila-Costas & M. G. Edmunds 1992; M. S. Oey & R. C. J. Kennicutt 1993; S. F. Sánchez 2020). Studies with large samples of galaxies, such as the Calar Alto Legacy Integral Field Area (CALIFA) survey or the Sloan Digital Sky Survey (SDSS), have measured a characteristic gradient of approximately -0.1 dex/R_e from their distribution of slopes, where R_e is the disk effective radius (S. F. Sánchez et al. 2014; L. Sánchez-Menguiano et al. 2016b; T. Parikh et al. 2021). However, individual galaxies can have multiple metallicity slopes within the disk of the galaxy (L. Sánchez-Menguiano et al. 2018).

In our current understanding of galaxy evolution, gas from the regions surrounding galaxies, namely, the circumgalactic medium (CGM) or intergalactic medium, is accreted onto the outer parts of the galactic disk (R. Roskar et al. 2010; A. S. Font et al. 2011; C. N. Lackner et al. 2012; S. M. Moran et al. 2012; J. Sánchez Almeida et al. 2014). The accretion process is thought to be crucial to supplying galaxies with gas to continue forming stars. However, directly observing active gas accretion is challenging due to the low densities in the CGM.

Indirect evidence of gas accretion can be found via observations of the bright star-forming regions within galactic disks since inflows of ex situ gas can have a chemical composition different from that of disk gas. If the newly introduced gas is metal poor, it can dilute the metal content of the star-forming regions (B. M. Tinsley 1973; F. Bournaud & B. G. Elmegreen 2009; A. Dekel et al. 2009; F. Vincenzo et al. 2016a; Z. J. Pace et al. 2021). The diluted regions can then become anomalies in the metallicity pattern across the galaxy. Several studies of individual galaxies have found these anomalously low-metallicity (ALM) regions (J. Sánchez Almeida et al. 2014; J. C. Howk et al. 2018a, 2018b; Y. Luo et al. 2021; M. Ju et al. 2022). Recently, integral-field surveys with more statistical robustness, like the Mapping Nearby Galaxies at Apache Point Observatory (MaNGA) survey, have found a large sample of ALM regions with a preference for low-mass galaxy hosts ($<10^{10} M_{\odot}$; H.-C. Hwang et al. 2019). Theory and a growing amount of observations suggest that these ALM regions are a result of low Z gas accretion into the disk that forms young stars (J. C. Howk et al. 2018a; H.-C. Hwang et al. 2019; L. Scholz-Diaz et al. 2021).

1.1. NGC 99

As a pilot study, we selected NGC 99 to explore radial metallicity gradients, search for ALM H II regions, and investigate a resolved fundamental metallicity relation (FMR). NGC 99 is a star-forming spiral galaxy at a distance of 79.4 Mpc. As part of the Deciphering the Interplay between the Interstellar medium, Stars, and the Circumgalactic medium (DIISC) survey (S. Borthakur et al. 2024), NGC 99 has extensive multiwavelength data coverage allowing us to probe the chemical compositions of its star-forming regions, ISM, and CGM and connect that information to other physical properties such as stellar mass ($M_{\star}$) and SFR. To do this, we combine data from the Very Large Array, the Vatican Advanced Technology Telescope, the Hubble Space Telescope, the LBT, and our newly obtained multiobject spectra from the MMT. M. Padave et al. (2024a) recently measured the global stellar mass ($M_{\star,\mathrm{global}}$) and star formation rate ($\mathrm{SFR}_{\mathrm{global}}$) of NGC 99 to be $4.17 \times 10^{10} M_{\odot}$ and $2.45\, M_{\odot}\,\mathrm{yr}^{-1}$, respectively. H. B. Gim et al. (2024, in preparation) found the total H I mass to be $1.68 \times 10^{10} M_{\odot}$. Other properties of NGC 99 can be found in Table 1.

We combine optical spectra of 26 H II regions with optical band and radio H I 21 cm imaging to study the disk of NGC 99. We also probe the CGM of the galaxy at 159 kpc from its center with a UV-bright QSO sightline. The paper is organized as follows. In Section 2, we describe the suite of data available and its reduction. In Section 3, we analyze radial gradients of the dust content and metallicity. In Section 4, we discuss our results in the context of other studies, explore chemical evolution models, and derive a resolved FMR. We summarize our findings in Section 5.

2. Observations and Data Analysis

2.1. Optical Spectroscopy of H II Regions

We obtained multislit spectra for NGC 99 using the new spectroscopy instrument, Binospec, on the MMT 6.5 m telescope located on Mount Hopkins in Arizona. The observations were taken over a period of four nights between 2020 September and 2021 November with an average seeing of $1\overset{''}{.}15$. A catalog of far-ultraviolet (FUV) bright targets was created using `SExtractor` (E. Bertin & S. Arnouts 1996) on an archival FUV image from the Galaxy Evolution Explorer (GALEX; D. C. Martin et al. 2005; P. Morrissey et al. 2007). The image is presented in M. Padave et al. (2024a). Regions with a FUV magnitude brighter than 25 were added to the catalog. UV regions are generally spatially correlated with Hα regions as both are used as star formation indicators. Hence, we are targeting and detecting H II regions. The `BinoMask` software (J. Kansky et al. 2019) then automatically selected targets from the catalog by optimizing for the highest number of targets per mask design and placing slits to avoid the effects of differential atmospheric refraction. `BinoMask` selected a total of 31 UV-bright H II regions to observe.

Table 1
Properties of NGC 99

Parameter	Value
R.A.[a] (α_{2000})	$00^{h}23^{m}59\overset{s}{.}422$
Decl.[a] (δ_{2000})	$+15°46'13\overset{''}{.}04$
Morphological Type[b]	SABc
Inclination[c]	20°
Redshift[d]	0.01771
Distance[e]	79.4 Mpc
Stellar mass ($M_{\star,\mathrm{global}}$)[c]	$4.17 \times 10^{10}\, M_{\odot}$
R_{25}[c]	11.46 kpc
R_{e}[c]	8.51 kpc
$E(B-V)$[f]	0.0481
$\mathrm{SFR}_{\mathrm{global}}$[g]	$2.45\, M_{\odot}\,\mathrm{yr}^{-1}$
$R_{\mathrm{H\,I}}$[h]	45.8 kpc
H I mass[h]	$1.68 \times 10^{10}\, M_{\odot}$
Circular velocity[h]	$292\ \mathrm{km\ s}^{-1}$
Gas dispersion[i]	$14\ \mathrm{km\ s}^{-1}$
Halo mass[j]	$5.0 \times 10^{11}\, M_{\odot}$
Virial radius[j]	207 kpc

Notes.

[a] M. F. Skrutskie et al. (2006).

[b] R. J. Buta (2019).

[c] M. Padave et al. (2024a).

[d] C. M. Springob et al. (2005).

[e] Calculated using the distance modulus value from S. F. Sánchez et al. (2012).

[f] E. F. Schlafly & D. P. Finkbeiner (2011).

[g] Estimated from far-ultraviolet and 22 μm data adopted from M. Padave et al. (2024a).

[h] Based on the peak of the distribution of velocity dispersions in the Very Large Array D-configuration H I image. We adopt the peak value because some of the values at the central regions are impacted by beam smearing of the steeply varying rotation curve.

[i] Based on Very Large Array D-conf. observations (H. B. Gim et al. 2024, in preparation).

[j] Halo mass and virial radius were estimated from the stellar mass using prescriptions by A. V. Kravtsov et al. (2018) and applying modifications based on the findings of R. Mandelbaum et al. (2016). The full sample will be described in S. Borthakur et al. (2024).

Each mask was observed for a total of 2400 s using four exposures of 600 s each during the same night. We used the 270 lines mm^{-1} grating of Binospec with a central wavelength of 5800 Å for each slit at a dispersion of 1.3 Å pix^{-1}. This allowed us to cover the entire wavelength range of emission lines observed from 3900 to 9240 Å in one setting. The data were reduced using the Binospec Data Reduction Pipeline, which carried out the bias correction, flat-fielding, wavelength calibration, relative flux correction, coaddition, and extraction to 1D spectra (J. Kansky et al. 2019). Of the 31 regions observed, the spectra of 26 regions had measurable emission lines. The slit locations can be seen in Figure 1. Figure 2, a spectrum of region 16, shows a representative H II region

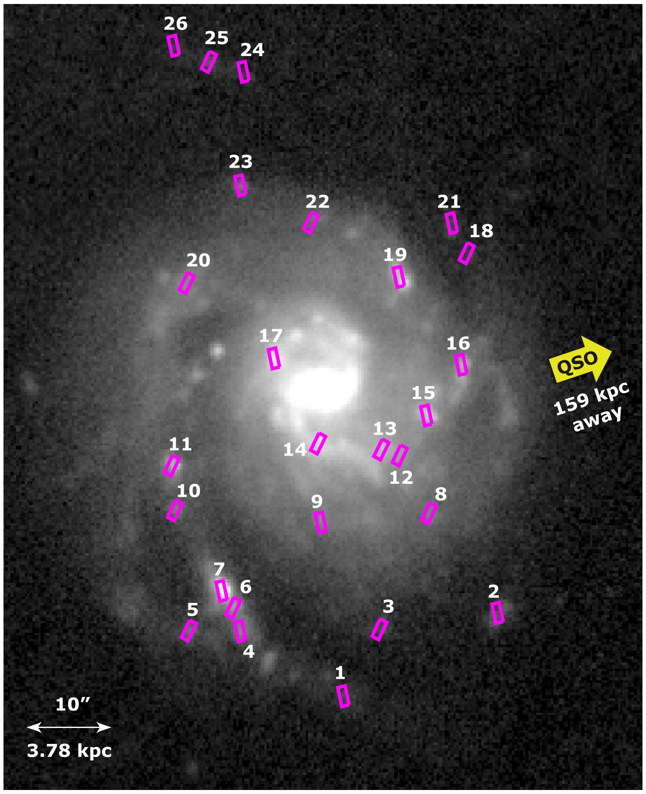

Figure 1. A r-band image of NGC 99 obtained at the Vatican Advanced Technology Telescope with all the included Binospec slits placed on the H II regions labeled by their assigned number. The yellow arrow points in the direction of QSO SDSS J002330.58+154744.9, which is a projected distance of 159 kpc away from the galaxy center.

spectrum produced by the Binospec instrument with the lines we aim to measure.

After correcting the spectra for redshift, emission lines were found using the find_lines_derivative method from the `specutils` python package (N. Earl et al. 2022) and identified by matching the line center with an emission line database. The local continuum level within a $\sim$100 Å window was measured using `specutils`' fit_generic_continuum function and subtracted from each emission line. The total integrated flux of each line was then calculated using the amplitude and standard deviation of a modeled Gaussian. Using pyFIT3D (E. A. D. Lacerda et al. 2022), we modeled the stellar spectrum of our H II region with the strongest continuum level to investigate the effect of stellar absorption, which we found to be minimal. Therefore, for other targets where the continuum is weaker, the stellar absorption is not modeled as it would not be significant compared to the strength of the emission lines.

Our absolute flux calibration has some uncertainty. However, this should have no impact on our metallicity measurements and very little on the Balmer decrement. To ensure an accurate SFR estimate, we cross calibrated our Hα fluxes with VATT narrowband Hα imaging (M. Padave et al. 2024b). The Hα flux of each region is reported in Table A1. We investigated the shape of the Hα emission line, which is the strongest line in these spectra, to look for evidence of multiple component emission. We found that all but one of the emission lines fit well with a single Gaussian profile. The spectrum from Region 2 shows a slight wing toward shorter wavelengths.

2.2. Optical g- and r-band Data

Optical continuum g- and r-band imaging of NGC 99 was obtained on UT 2020 October 7 using the VATT4k CCD imager at the 1.8 m Vatican Advanced Technology Telescope (VATT) operated by the Mount Graham Observatory. The total exposure times in g and r are 600 and 1200 s, respectively. The observation setup and data reduction are described in M. Padave et al. (2024a).

We utilize the r-band image and `statmorph` (V. Rodriguez-Gomez et al. 2019) to estimate position angle, ellipticity, and inclination. We then use these parameters and the R.A. and decl. of each region to calculate the H II region's semimajor axis value. We assume the galaxy to be circular in projection, thus taking the semimajor value to be the H II region's galactocentric radius.

2.3. VLA H I 21 cm Data

The H I 21 cm emission from NGC 99 was observed with the Karl G. Jansky Very Large Array (VLA) in the D-configuration as a part of the VLA-DIISC project (H. B. Gim et al. 2024, in preparation). The observations were performed from 2019 November 9 through November 16 (program ID: 19B-183) for a total of 6.5 hr with a channel spacing of 5.208 kHz within the bandwidth of 16 MHz at the central frequency of 1395 MHz. The data reduction was carried out with the Common Astronomy Software Application (CASA; J. P. McMullin et al. 2007) version 5.6.1 according to the general reduction schemes for H I spectroscopy. The absolute flux density scale and bandpass were calibrated using 3C 48, while the complex gain was calibrated using J2340+1333. Hanning smoothing was applied to the data to mitigate Gibbs ringing phenomena, resulting in an effective velocity resolution of 2.2 km s^{-1}, doubling the original velocity width.

The image cube was made by the CASA task *tclean* with a pixel size of 6″, the Briggs weighting function, and a robust value of 0.5 for the optimal sensitivity and synthesized beam size. The cleaning was performed until the maximum residual reached 1.5σ, where σ is the rms noise in the image. The image cube was spatially smoothed to the synthesized beam size of $50\farcs5 \times 47\farcs5$ over all the channels. The final image cube has a sensitivity of 0.69 mJy beam^{-1} (2.2 km s^{-1})$^{-1}$ corresponding to a column density of 6.81×10^{18} cm^{-2}.

The H I 21 cm emission from NGC 99 was recovered by the Source Finding Application-2 (SoFiA-2, P. Serra et al. 2015; T. Westmeier et al. 2021) above 3σ, where it was found within the velocity range of 5125.4–5312.3 km s^{-1}. The velocity width of the H I spectrum is $W_{50} = 130.54$ and $W_{20} = 154.78$ km s^{-1} at 50% and 20% of the maximum intensity, respectively. The H I mass was estimated to be $M_{\rm HI} = (1.68 \pm 0.03) \times 10^{10} M_{\odot}$ assuming a luminosity distance of 79.4 Mpc.

2.4. COS Spectra

The ultraviolet spectrum of the quasi-stellar object (QSO) SDSS J002330.58+154744.9, which is at an impact parameter of 159 kpc from the center of NGC 99, was obtained using the G130M medium resolution grating of the Cosmic Origin Spectrograph (COS; S. Osterman et al. 2011; J. C. Green et al. 2012) on board the Hubble Space Telescope under observing program GO-14071 (PI: Borthakur). After processing with the standard COS pipeline, the multiple G130M spectra were coadded and binned by 3 pixels, resulting in a spectral bin size

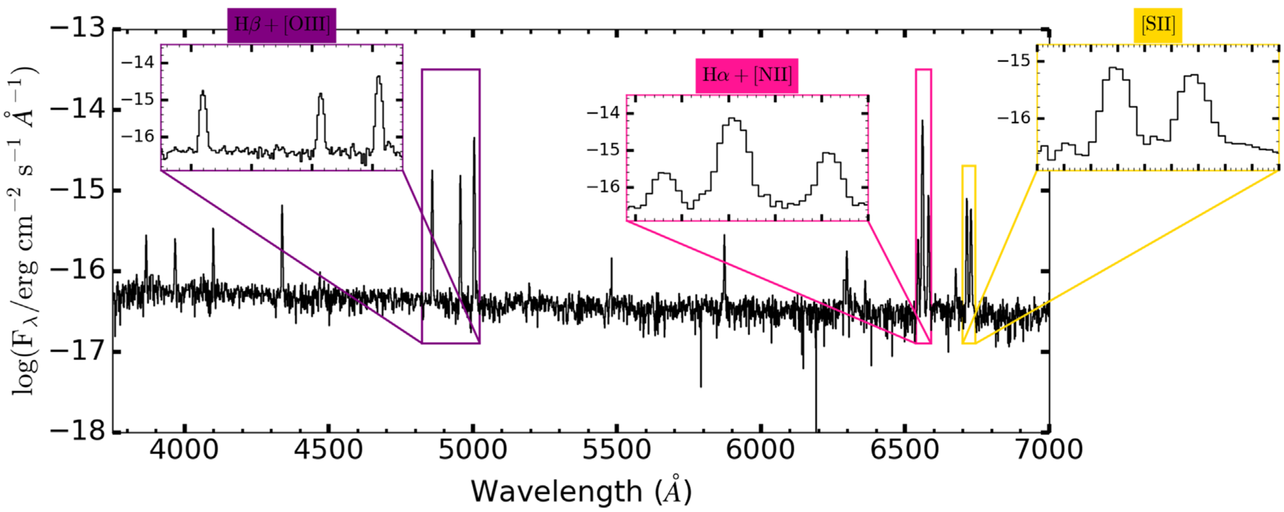

Figure 2. A typical MMT/Binospec spectrum of an H II region in NGC 99. The flux is shown in log scale to show the level of the underlying stellar continuum. The three insets highlight the emission lines of interest in this study.

Table 2
Measurements from QSO Absorption Spectroscopy Tracing the CGM of NGC 99

Species	λ_{rest} (Å)	W_{rest}[a] (mÅ)	Component Label	Centroid[b] (km $\mathrm{s^{-1}}$)	Doppler b (km $\mathrm{s^{-1}}$)	log N (log $\mathrm{cm^{-2}}$)
H I	1215	513 ± 52	(A)	−44 ± 8	42 ± 0.1	⩾14.4 ± 0.2
…	…	…	(B)	34 ± 14	17 ± 42	13.2 ± 0.6
…	…	…	(C)	99 ± 11	15 ± 41	13.1 ± 0.5
…	…	…	(D)	366 ± 21	30 ± 1	13.1 ± 0.4
Si II	1302	⩽119[c]	…	…	…	⩽ 12.86
Si III	1206	⩽144[c]	…	…	…	⩽ 12.83
Si IV	1393	⩽144[c]	…	…	…	⩽ 13.21
C II	1334	⩽143[c]	…	…	…	⩽ 13.85
N V	1238	⩽124[c]	…	…	…	⩽ 13.77

Notes.
[a] Equivalent widths as estimated directly from the data. The error is calculated from both continuum fitting and statistical errors.
[b] Velocity centroid values are reported with respect to the rest frame of NGC 99 ($z = 0.0177$).
[c] The values represent 3σ upper limits.

of $\sim$7 km $\mathrm{s^{-1}}$ in the observed wavelength coverage of $\lambda = 1152$–1453 Å. All absorption features associated with the QSO, the Milky Way's ISM, and NGC 99's CGM were identified through visual inspection. We detected H I λ1215 (Lyα) in absorption in the CGM of NGC 99.

To fit the Lyα profile, we determined the continuum bracketing the absorption by using feature-free regions within ±1000 km $\mathrm{s^{-1}}$. The continuum was estimated using a Legendre polynomial of order 2 using the procedure of K. R. Sembach et al. (2004), which was then used to produce the normalized spectrum. We fit Voigt profiles to each feature using the software of E. L. Fitzpatrick & L. J. Spitzer (1997), and techniques similar to J. Tumlinson et al. (2013). These fits derived the velocity centroids, Doppler b-values, and column densities for the profile, which are listed in Table 2. The measurement uncertainties were derived using the error analysis methods of K. R. Sembach & B. D. Savage (1992).

We find four components (labeled A–D) of Lyα and fit each separately. Due to saturation, the best-fit Voigt profile for the dominant component (A) gives a lower limit on the column density of $N(\mathrm{H\,I}) > 2.69 \times 10^{14}\ \mathrm{cm^{-2}}$ (Figure 3). The three weaker components (B–D) have column density estimates of $N(\mathrm{H\,I}) = 1.67 \times 10^{13}$, 1.13×10^{13}, and $1.20 \times 10^{13}\ \mathrm{cm^{-2}}$. The centroid for the dominant component is −44 km $\mathrm{s^{-1}}$ offset

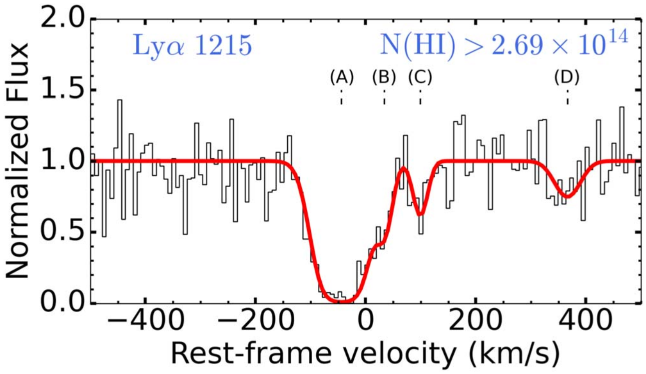

Figure 3. COS spectra of the Lyα transition plotted at the rest frame of NGC 99 ($z = 0.0177$). The best combined profile is plotted in red, and the resulting column density estimate is shown in the upper right. The dominant absorption component (A) is −44 km $\mathrm{s^{-1}}$ offset from the systemic velocity of the galaxy, with three weaker components (B–D) located at 34 km $\mathrm{s^{-1}}$, 99 km $\mathrm{s^{-1}}$, and 366 km $\mathrm{s^{-1}}$. Lyα is the only detected species associated with the galaxy's CGM. Measurements for Lyα and upper limits for the metal lines are presented in Table 2.

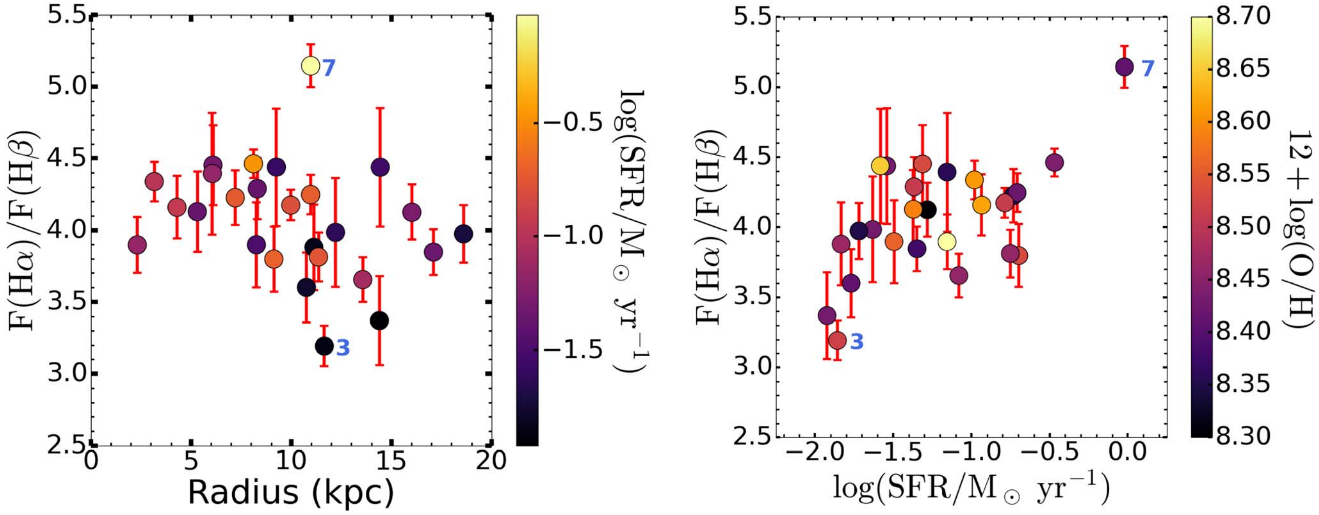

Figure 4. The Balmer decrement of each H II region as a function of its galactocentric radius (left) and star formation rate (right). The associated error bars are overplotted in red. The observed H II regions within 10 kpc of the center of NGC 99 show a flat radial distribution. H II regions outside of 10 kpc show wide scatter.

from the systemic velocity of NGC 99, while the weaker components are located at 34 km s^{-1}, 99 km s^{-1}, and 366 km s^{-1}.

3. Results

3.1. Dust Extinction

We investigated the dust content of the H II regions using the Balmer decrement, F(Hα)/F(Hβ) flux, across the galaxy. The Balmer decrement of each region is listed in Table A1. The left panel of Figure 4 shows the Balmer decrement for the 26 H II regions as a function of galactocentric radius. All the points show F(Hα)/F(Hβ) values greater than the expected intrinsic value of 2.86 from Case B recombination in the absence of dust. Within 10 kpc of the center, the regions show a flat Balmer decrement, while at radii greater than 10 kpc, the points show a wide scatter. One point in particular, region 7 at 11 kpc, shows a high F(Hα)/F(Hβ) value of ≈5.14, while the lowest value of 3.19 was observed in region 3 at 11.7 kpc.

The right panel of Figure 4 reveals a connection between the Balmer decrement and the SFR of the H II regions where a higher SFR is associated with higher Balmer ratios. From the Schmidt–Kennicutt (SK) law, we expect higher SFRs with larger cold gas surface densities, $\Sigma_{\rm gas}$ (M. Schmidt 1959; R. C. J. Kennicutt 1998). For a fixed dust-to-mass ratio, the dust column density and the gas column densities are coupled; the observed correlation is not surprising.

Dust has also been used as a proxy for gas metallicity; however, the color-coded points of the right panel of Figure 4 reveal that the Balmer decrement of the H II regions has little dependence on the gas-phase metallicity of the regions. Therefore, we conclude that metallicity is not the primary factor affecting the trend between the dust content and the SFR.

3.2. Gas-phase Metallicity

We investigate how the metallicity of the H II regions in the galaxy varies as a function of galactocentric radius. We measured the flux of the strong emission lines Hα, Hβ, [O III] λ5007, [N II]λ6583, and [S II]λ6717, 31. The ratios of these fluxes provide metallicity indicators N2 and O3N2, which are defined as

$$\mathrm{N2} = \log\left(\frac{[\mathrm{N\,II}]\,\lambda6583}{\mathrm{H}\alpha}\right) \quad (1)$$

$$\mathrm{O3N2} = \log\left(\frac{[\mathrm{O\,III}]\,\lambda5007}{\mathrm{H}\beta}\frac{\mathrm{H}\alpha}{[\mathrm{N\,II}]\,\lambda6583}\right), \quad (2)$$

where the lines refer to line fluxes (L. Searle 1971; D. Alloin et al. 1979; G. Denicolo et al. 2002; L. J. Kewley & M. A. Dopita 2002; M. Pettini & B. E. J. Pagel 2004; T. Nagao et al. 2006; R. A. Marino et al. 2013; M. A. Dopita et al. 2016; M. Curti et al. 2017; F. Bian et al. 2018; R. Maiolino & F. Mannucci 2019; M. Curti et al. 2020). The N2 and O3N2 values for each region are given in Table A1. Both the indicators have the benefit of being insensitive to dust attenuation since the two lines in each line ratio (Hα/[N II] λ6583 and [O III]λ5007/Hβ) are close in wavelength space (~20 Å). The indicators serve well as proxies for the metallicity of the systems and can be converted into oxygen gas-phase metallicities 12 + log(O/H). We follow the prescription from M. Curti et al. (2020) to obtain gas-phase metallicities.

Figure 5 shows N2 and O3N2 as a function of galactocentric radius with the corresponding gas-phase metallicity on the right y-axis. The black solid line shows the best linear fit between the galactocentric radius and gas-phase metallicity, while uncertainty is given by the shaded regions. The slope, intercept, and associated errors were estimated using `polyfit` from NumPy. When fitting for 12 + log(O/H) instead of N2 and O3N2 as a function of galactocentric radius, the radial gradients are −0.017 and −0.020 dex kpc^{-1}, respectively. Further information can be found in Table A2. The filled circles are color coded by $|V_{\mathrm{H}\alpha} - V_{\mathrm{HI}}|$, the absolute difference between the centroid of the Hα emission line and the mass-weighted H I 21 cm velocity of each region. Both indicators show the expected trends of decreasing metallicity with increasing radius in general, with N2 and O3N2 having a Spearman-ρ value of −0.60 and −0.63, respectively.

Interestingly, two regions at radii 6.1 and 7.2 kpc (labeled 15 and 19 in Figure 1, respectively) show an abnormal drop in

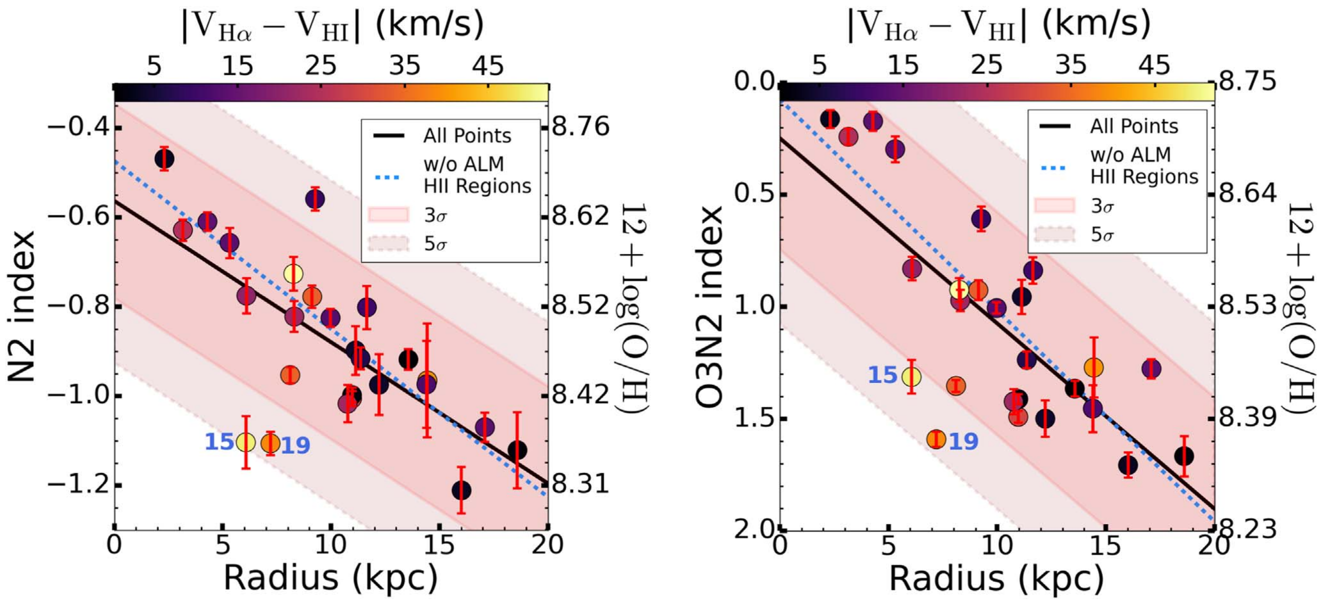

Figure 5. The metallicity radial gradient from both the N2 (left) and the O3N2 (right) indices. The right-side y-axis in both panels shows the corresponding gas-phase metallicity calculated from the calibration equations derived in M. Curti et al. (2020). The black solid line shows the best linear fit to all of the data, and the red and dark red shaded regions signify the 3σ and 5σ, respectively, confidence intervals of the fit. For $y = 12 + \log(O/H)$, the slopes of the fit are -0.017 and -0.020 dex kpc^{-1}, respectively. The color bar shows the absolute difference between the Hα emission line velocity offset and the mass-weighted H I 21 cm velocity of the ISM in the region. Regions 15 and 19, which are labeled and are at 6.1 and 7.2 kpc, show both anomalously low metallicity and a high velocity difference. The blue line shows the fit without the two ALM regions. The fits (slopes and intercepts) are presented in Table A2.

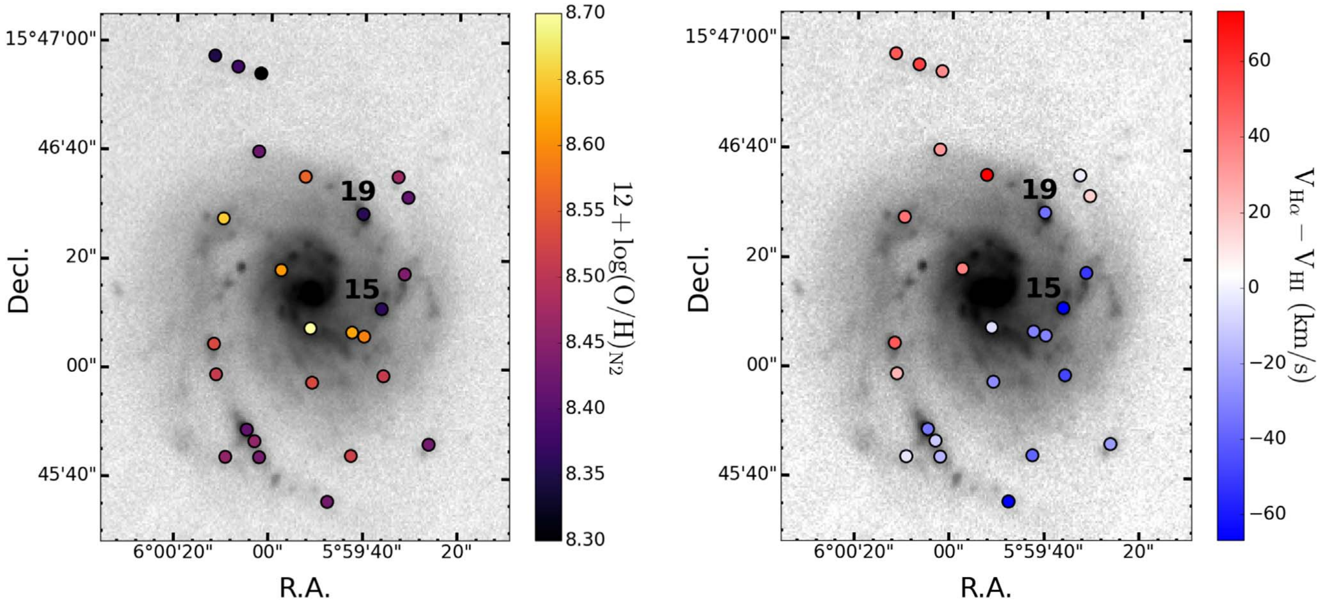

Figure 6. r-band images of the NGC 99 with the locations H II regions indicated by the circles, which are color coded based on their gas-phase metallicity (left) and velocity offset of the Hα emission line (right). Regions 15 and 19 show abnormally low metallicities and high velocities relative to their surrounding regions.

metallicity compared to others at similar radii, regardless of which metallicity indicator is used. These regions are more than 3σ below the linear fits shown in Figure 5. In addition, these regions also show a high velocity offset between $V_{H\alpha}$ and V_{HI}. Both trace the spiral arms and, on visual inspection, do not show any morphological differences.

We performed a Cook's distance statistical outlier test and confirmed that these regions are outliers in the data. Masking the two ALM H II regions, we refit the data and found that the radial gradient for both N2 and O3N2 became steeper by 0.03 dex. The new gradients are shown by the blue dashed line in Figure 5.

Figure 6 shows the spatial locations of the H II regions with filled circles color coded based on their metallicity and velocity offset of the Hα emission line from the ISM kinematics. Region 15 lies in one of the spiral arms of NGC 99 and is surrounded by points with higher metallicity while also having a higher velocity offset. Region 19 shows a negative velocity offset despite its colocated ISM showing a positive velocity consistent with rotation. Combining the metallicity and velocity information presented in Figure 5, we suggest that the star formation in these regions is fueled by low-metallicity gas that has been accreted into the disk of the galaxy.

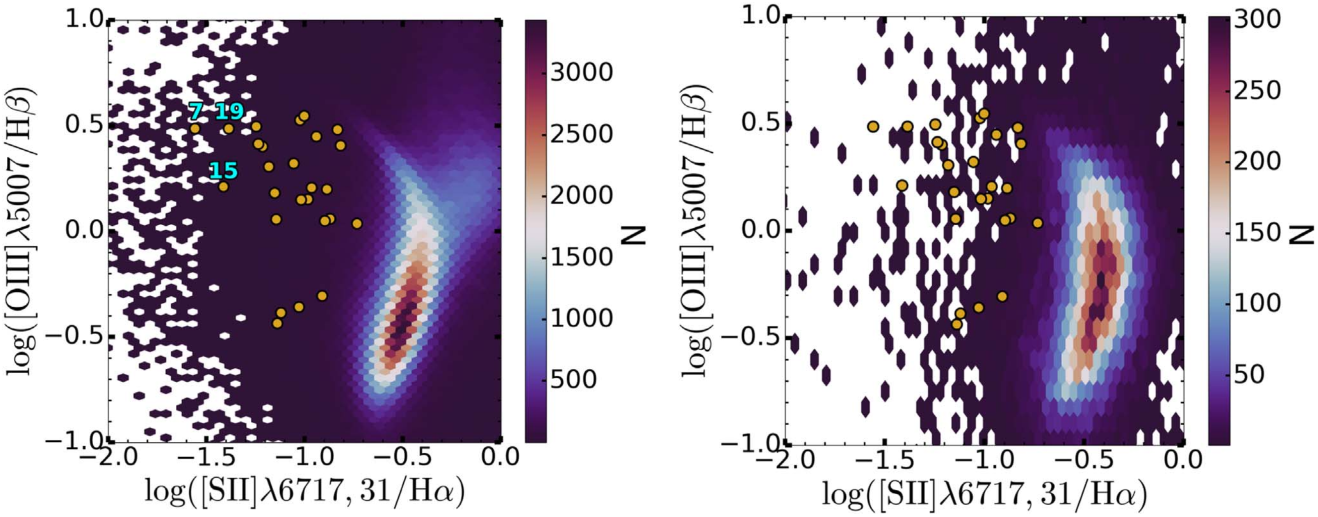

Figure 7. Distribution of 26 H II regions (filled gold circles) on a background of hexagon bins from SDSS-DR8 galaxies (left) and from CALIFA H II regions (right). The color bar shows the number of galaxies or H II regions in each bin. The data points show a 0.5–1.0 dex offset in [S II] from the majority of SDSS galaxies and CALIFA H II regions.

Alternative explanations for the ALM H II regions may be azimuthal and arm–interarm variations in the oxygen abundance and deviations from the general radial profiles, which have been observed and described in many galaxies (R. C. J. Kennicutt & D. R. Garnett 1996; P. Martin & J. Belley 1996; B. Cedrés & J. Cepa 2002; F. F. Rosales-Ortega et al. 2011; B. Cedrés et al. 2012; Y. Li et al. 2013; S. F. Sánchez et al. 2015; L. Sánchez-Menguiano et al. 2016a, 2017, 2019). It is also possible that these H II regions are extraplanar and look like part of the disk due to projection effects. However, that is not likely in this case as NGC 99 is almost face-on ($i = 20°$), so projection effects are minimal. Therefore, we conclude that the ALM H II regions are due to the accretion of low-metallicity gas. Similar conclusions were also made by other recent studies, such as J. C. Howk et al. (2018a), H.-C. Hwang et al. (2019), and L. Scholz-Diaz et al. (2021).

3.3. [S II] Deficiency

We make measurements of the [S II]λ6717, 31 emissions lines and measure [S II]-based metallicity indicators such as S2, N2S2Hα, and RS32 (G. Denicolo et al. 2002; S. Y. Yin et al. 2007; M. A. Dopita et al. 2016; M. Curti et al. 2017; R. Maiolino & F. Mannucci 2019; M. Curti et al. 2020). For example, the S2 index, defined as

$$\mathrm{S2} = \log\left(\frac{[\mathrm{S\,II}]\lambda6717,\,31}{\mathrm{H}\alpha}\right), \tag{3}$$

shows no radial dependence with galactocentric radius. Overall, the [S II]-based indicators show large variation compared to N2 or O3N2.

To investigate it further, we constructed a line ratio diagram (Figure 7) using the line ratios of [O III]/Hβ and [S II]/Hα from our 26 H II regions. The left panel of Figure 7 shows SDSS galaxies from H. Aihara et al. (2011) as the binned background, while the right panel background shows H II regions from the CALIFA survey (C. Espinosa-Ponce et al. 2020). Our regions show a deficiency between 0.5 and 1.0 dex from the expected value of S2 for a set value of the [O III]/Hβ ratios, regardless of which sample we compare to. Our observations are consistent with those observed by J. Wang et al. (1997), albeit for galaxies. They inferred that this [S II] deficiency is caused by the leaky H II regions where Lyman-continuum (LyC) photons are escaping into the surrounded ISM. Since [S II] is mostly produced at the boundary between the ionized and neutral zones of H II regions, the width of our slits, 1″ or 0.378 kpc, may not encompass the entirety of the [S II] produced due to the interaction of LyC photons with neutral gas (E. W. Pellegrini et al. 2012). For this reason, we refrain from using any indicator involving [S II].

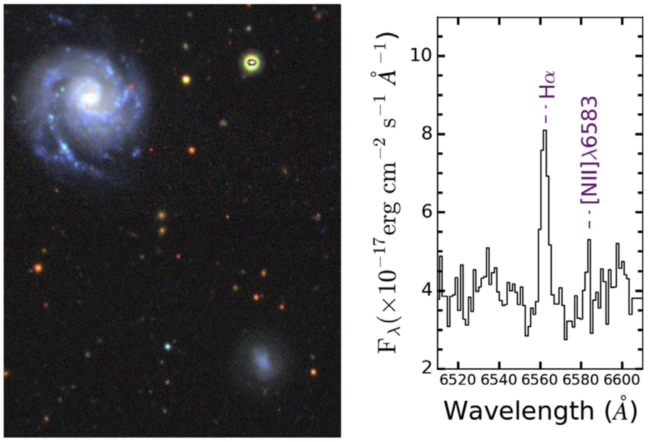

Figure 8. Optical image (left) of NGC 99 (top left of image) and its companion J002353.17+154356.8 (bottom right of image) from the DESI Legacy Survey (A. Dey et al. 2019). The projected distance between the objects is 57 kpc. (right) The optical spectrum showing the Hα and [N II]λ6583 emission lines of J002353.17+154356.8 obtained with the MMT using the Binospec instrument. The redshift was measured to be 0.01747.

3.4. Spectroscopic Observations of Neighboring Dwarf Galaxy

SDSS J002353.17+154356.8 is a dwarf galaxy located 57 kpc away from NGC 99 in projection. The left panel of Figure 8 shows an optical image of NGC 99 with SDSS J002353.17+154356.8 near the bottom right corner of the image. We detail its properties in Table A3. While observing NGC 99 with the MMT as described in Section 2.1, we also placed a slit on the center of SDSS J002353.17+154356.8 oriented along its major axis and obtained a

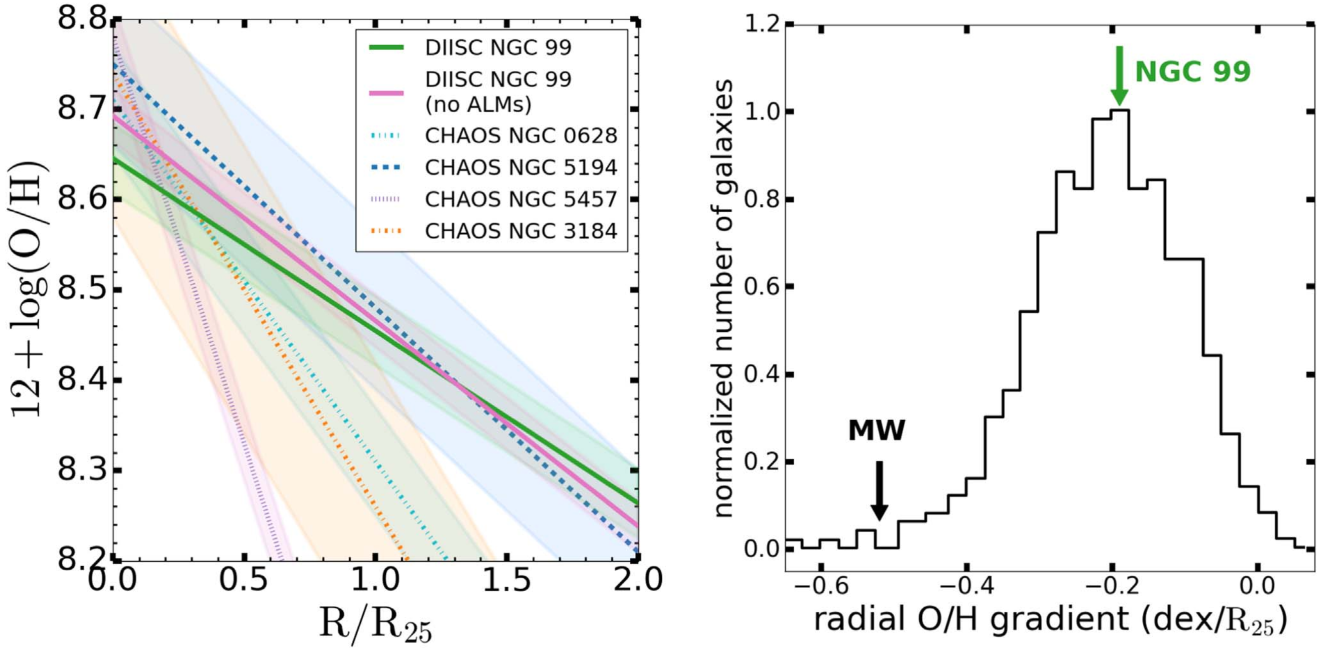

Figure 9. (Left) The metallicity radial metallicity profiles found from our 26 H II regions in dex$/R_{25}$ in comparison to the four CHAOS galaxies from D. A. Berg et al. (2020). NGC 99 (green and pink solid lines) has a shallower slope than all of the CHAOS galaxies. The shaded regions indicate the 1σ error. (Right) A histogram of metallicity gradients in 504 galaxies found by L. S. Pilyugin et al. (2023). The green arrow indicates where NGC 99 fits in this distribution. The black arrow indicates the metallicity gradient observed in the Milky Way.

spectrum with measurable emissions lines present. The right panel of Figure 8 shows a cutout of the optical spectrum of the dwarf galaxy. The spectrum was reduced using the same procedure as the spectra in NGC 99. By measuring the center of the Hα emission line, we found a redshift of 0.01747, which is slightly lower than the redshift of NGC 99. The close proximity of the dwarf galaxy leads us to believe it is a satellite of NGC 99. Shifting the spectrum into NGC 99's frame of reference, we measured a velocity offset of -74.51 km s^{-1} with respect to NGC 99. We calculated that the dwarf galaxy has an N2 value of -0.46 corresponding to $12 + \log(\mathrm{O/H}) = 8.71$ (M. Curti et al. 2020).

We utilize the $M_\star$ map from M. Padave et al. (2024a) and the H I 21 cm image from H. B. Gim et al. (2024, in preparation) to measure the $M_\star$ and H I mass of the dwarf galaxy to be $8.62 \times 10^8\,M_\odot$ and $5.8 \times 10^9\,M_\odot$, respectively. The stellar mass of J002353.17+154356.8 is comparable to the Small Magellanic Cloud (SMC; $M_{\star,\mathrm{SMC}} = 3.1 \times 10^8\,M_\odot$) but has an H I mass an order of magnitude higher than the SMC's gas mass ($M_{\mathrm{gas,SMC}} = 4.2 \times 10^8\,M_\odot$; G. Besla 2015). J002353.17+154356.8 does not show any signs of tidal disruption due to its host galaxy, so we can conclude that the presence of this dwarf galaxy does not affect any of the properties of NGC 99.

4. Discussion

4.1. Metallicity Radial Gradient Comparison

We compared our radial metallicity gradient to four galaxies from the CHemical Abundances Of Spirals (CHAOS) project that are similar in mass to NGC 99. D. A. Berg et al. (2020) measured the radial metallicity gradient of NGC 0628, NGC 3184, NGC 5194, and NGC 5457 using the direct method to measure the metallicity of multiple H II regions observed with the Multi-Object Double Spectrographs (MODS; R. W. Pogge et al. 2010) on the Large Binocular Telescope (LBT). The left panel of Figure 9 shows the metallicity distribution of NGC 99 and the four CHAOS galaxies as a function of galactocentric radius normalized by each galaxy's isophotal radius (R_{25}). In comparison to NGC 99, the four CHAOS galaxies are less massive ($10.0 < \log M_\star(M_\odot) < 10.5$) and much closer ($7.2 < D$(Mpc) < 11.7). NGC 99 has a shallower slope than every CHAOS galaxy, even when masking the ALM H II regions (pink solid line). It should be noted that our observations of H II regions in NGC 99 only probe galactocentric radii between $2.3\ \mathrm{kpc} < R < 18.6$ kpc or $0.2 < R/R_{25} < 1.6$, in terms of R_{25}. Except for NGC 5457, observations of H II regions in the CHAOS galaxies also probe galactocentric radii down to similar radii ($\sim 0.1\,R/R_{25}$). Therefore, our linear fit and the fits from three of the CHAOS galaxies may be unreliable at $R < 0.2R/R_{25}$ as the fit may deviate from linear at lower radii. Additionally, the presence of the two ALM H II regions lowers the steepness of our slope. As noted in Section 3.2, removing regions 15 and 19 from the fit increased the steepness of the metallicity gradient.

Other studies with a large sample size have established a characteristic oxygen abundance gradient in galaxies (M. B. Vila-Costas & M. G. Edmunds 1992; S. F. Sánchez et al. 2014; F. Belfiore et al. 2017). Recently, L. S. Pilyugin et al. (2023) measured the radial metallicity gradient of 504 galaxies, of which 451 are MaNGA galaxies and 53 are nearby galaxies. The right panel of Figure 9 shows a histogram of the slopes measured by L. S. Pilyugin et al. (2023), with the black arrow showing where the Milky Way falls in the distribution. The mean of this distribution is -0.20 dex$/R_{25}$ with a scatter of -0.10 dex$/R_{25}$. The green arrow indicates the metallicity gradient of NGC 99 obtained from this work. Our Galaxy's gradient (-0.19 dex$/R_{25}$) approximately matches the mean found by L. S. Pilyugin et al. (2023). As a part of the CALIFA survey, S. F. Sánchez et al. (2014) measured the characteristic oxygen abundance of 306 galaxies using a catalog of over 7000 H II regions and found a characteristic gradient of

$-0.16\,\mathrm{dex}/R_{25}$ with a dispersion of $0.12\,\mathrm{dex}/R_{25}$. The gradient of NGC 99 falls within 1σ of the characteristic slope found by S. F. Sánchez et al. (2014). F. Belfiore et al. (2017) and N. F. Boardman et al. (2021) showed that the metallicity gradient of a galaxy depends on its stellar mass and size. For a galaxy with a total stellar mass of $\log_{10}(M_\star/M_\odot) = 10.6$, F. Belfiore et al. (2017) found that the corresponding metallicity gradient will be about $-0.14\,\mathrm{dex}/R_e$, which is identical to NGC 99's metallicity gradient in terms of its effective radius, R_e. Despite the difference in observational methods between multislit and integral-field units (IFUs), which S. F. Sánchez et al. (2014) and L. S. Pilyugin et al. (2023) utilize, NGC 99 falls within the dispersion of the distribution of radial gradients found by the IFU studies.

Although D. A. Berg et al. (2020), L. S. Pilyugin et al. (2023), and S. F. Sánchez et al. (2014) study different samples of galaxies and use different methods of measuring metallicities, it is clear that NGC 99 is comparable to most other star-forming galaxies in the local Universe. Therefore, the lessons learned from the study of this singular galaxy should be applicable to most other galaxies in the nearby Universe.

4.2. Chemical Evolution Modeling

Further indirect evidence of gas accretion can be found by modeling the chemical evolution of the H II regions. The simplest model is the closed-box model, in which it is assumed that no gas leaves or enters the system, and all the gas present is turned into stars over time. As star formation occurs, a portion of the gas mass is "locked" into lower-mass stars and stellar remnants, as these objects exist for much longer than the current age of the observable Universe. Supernovae explosions return another portion of gas mass to the ISM, increasing the local metallicity. This enrichment process is assumed to occur instantaneously. The yield (y) is used to characterize the amount of enrichment that occurred as it is defined to be the mass in metals returned to the ISM relative to the mass in stars formed for a whole population of stars (B. M. Tinsley 1980; A. Maeder 1992). Since we assume that the initial mass function (IMF) remains constant in time and no material enters or leaves the system, the yield produced by star formation remains constant for the galaxy.

Because the model is simple and makes many assumptions, it serves as a good basis to begin with. We will use it to observe where the assumptions break down and identify possible processes that may be at play. For all models, we assume the galaxy is not pre-enriched with metals. In the closed-box model, the effective yield (y_{eff}) is given by the equation

$$y_{\mathrm{eff}} \equiv \frac{Z_{\mathrm{gas}}}{\ln(1/f_{\mathrm{gas}})} \tag{4}$$

where the gas fraction $f_{\mathrm{gas}} \equiv M_{\mathrm{gas}}/(M_{\mathrm{gas}} + M_\star)$ and M_{gas} and $M_\star$ are gas mass and stellar mass, respectively. We utilize the $M_\star$ map of NGC 99 created using g- and r-band maps following the method described in M. Padave et al. (2024a) and estimate the $M_\star$ of each H II region by integrating over the area of the slit. We assume the present-day solar abundances of M. Asplund et al. (2021), where hydrogen and oxygen make up 74.38% and 0.58% of the total amount of M_{gas}, respectively. Therefore, $M_{\mathrm{gas}} = 1.345 M_{\mathrm{H}}$ following these abundances. We estimate M_{HI} from our VLA H I 21 cm surface density image by taking the pixel value at each slit location and multiplying it by the area of the slit. The $M_\star$ and M_{HI} of each H II region are shown in Table A4. We use single-dish CO measurements by A. Saintonge et al. (2017) to estimate a total $M_{\mathrm{H_2}}$ of $10^{9.18} M_\odot$ (after being distance corrected to 79.4 Mpc). The measurements were taken with the Institut de Radioastronomie Millimetrique (IRAM)-30 m telescope with a half-power beamwidth (HPBW) of 22″. These measurements are very close to those by X.-J. Jiang et al. (2015) who measured a value of $10^{9.13} M_\odot$ using the Submillimeter Telescope with an HPBW of 33″. This implies that most of the CO is located within 11″ of the center of NGC 99. In the absence of a molecular gas map, we assume the molecular gas to be spread uniformly within a circular region of 11″ (≈4.158 kpc) in radius, which yields a surface density of $27.9\,M_\odot\,\mathrm{pc}^{-2}$. Multiplying the surface density by the area of the slit, the molecular mass, $M_{\mathrm{H_2}}$, of each region is estimated to be $10^{6.99} M_\odot$. Therefore, $M_{\mathrm{H}} = M_{\mathrm{HI}} + M_{\mathrm{H_2}}$ for regions with $R < 4.158$ kpc and $M_{\mathrm{H}} = M_{\mathrm{HI}}$ for regions with $R \geqslant 4.158$ kpc. Finally, we convert our gas-phase metallicity measured via the N2 index to Z_{gas}, the metallicity by mass, via the following equation

$$\log(Z_{\mathrm{gas}}) = \log(\mathrm{O/H}) + 1.07, \tag{5}$$

where we assume solar gas-phase metallicity is 8.69 and $Z_{\mathrm{gas}} \equiv M_{\mathrm{O}}/M_{\mathrm{gas}}$.

In the closed-box model, the effective yield (y_{eff}) should match the "true" nucleosynthetic yield of oxygen, y_{O}, of the system, since all the gas present is converted into stars growing the metal content and decreasing the $M_\star$. y_{O} can range from 0.009 to 0.037 and is dependent upon metallicity and the assumed IMF (F. Vincenzo et al. 2016b; J. K. Barrera-Ballesteros et al. 2018; D. H. Weinberg et al. 2023). For this study, we adopt three true yields $y_{\mathrm{O}} = 0.009$, $y_{\mathrm{O}} = 0.014$, and $y_{\mathrm{O}} = 0.037$.

The left panel of Figure 10 shows a weak inverse correlation between metallicity and gas fraction. Previous studies have found this correlation to be stronger (J. K. Barrera-Ballesteros et al. 2018; P. Lagos et al. 2018; C. Tortora et al. 2022). In particular, J. K. Barrera-Ballesteros et al. (2018) found a tight relation between f_g and $12 + \log(\mathrm{O/H})$ using the MaNGA Survey and claimed gas fraction plays a vital role in local chemical enrichment. The right panel of Figure 10 shows that all of the regions have an effective yield lower than that of the true yields (the three lines in the figure). M. G. Edmunds (1990) showed that y_{eff} should be below the true yield if metals are lost by outflows or the ISM is diluted by inflows of metal-poor gas. Considering the ALM H II regions previously discussed in Section 3.2, the scenario of the inflow of low-metallicity gas diluting star-forming regions in the galaxy is strengthened by finding $y_{\mathrm{eff}} < y_{\mathrm{O}}$. The ALM H II regions (numbers 15 and 19) show particularly low effective yields of -2.90. Additionally, we find that the effective yields of the regions are roughly constant across the galactic disk, with the average being -2.60.

We now consider the effects of inflow on the chemical evolution of NGC 99 and adopt the accreting box model from J. Bovy (2023, in preparation). In this model, the effective yield is given by the equation

$$Z_{\mathrm{gas}} = y_{\mathrm{eff}}\left[1 - \exp\left(1 - \frac{1}{f_{\mathrm{gas}}}\right)\right] \tag{6}$$

where it is assumed that the accretion of gas is such that the total amount of gas in the box is constant in time. We tested

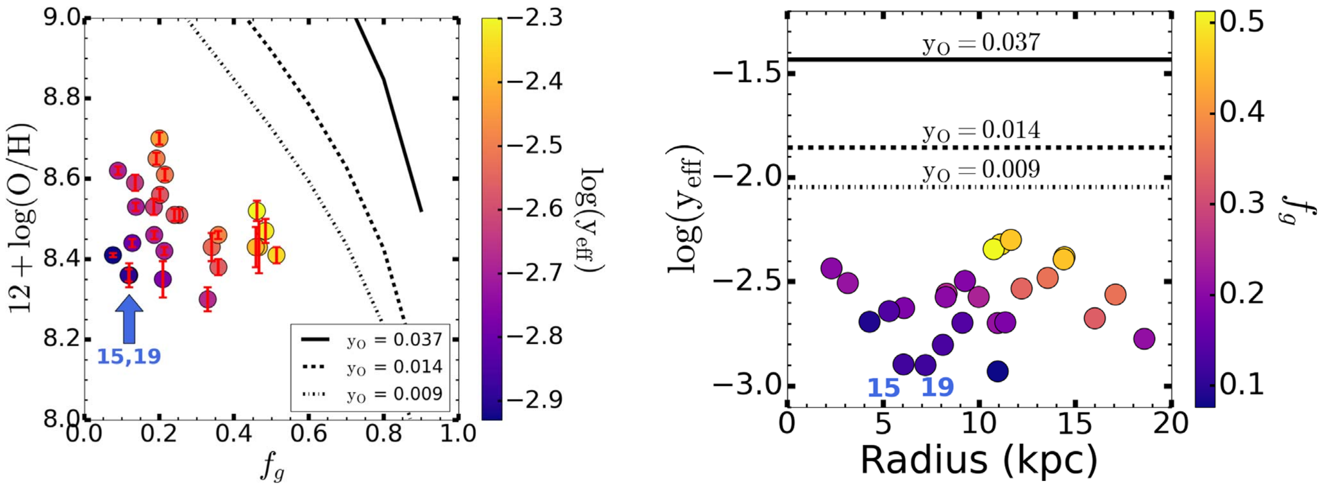

Figure 10. (Left) The gas-phase metallicity of the 26 H II regions is shown as a function of gas fraction with the points color coded by effective yield, $y_{\rm eff}$. A closed-box model is assumed to calculate effective yield. The lines show the true yield, y_O, found by C. Leitherer et al. (2014; dash) and F. Vincenzo et al. (2016b; solid and dashed–dotted, respectively). (Right) For the same H II regions, the effective yield is now shown as a function of galactocentric radius color coded by gas fraction. All of the H II regions have an effective yield lower than the true yield found by F. Vincenzo et al. (2016b). The effective yield is constant across the disk of the galaxy. The two ALM H II regions, numbers 15 and 19, are marked.

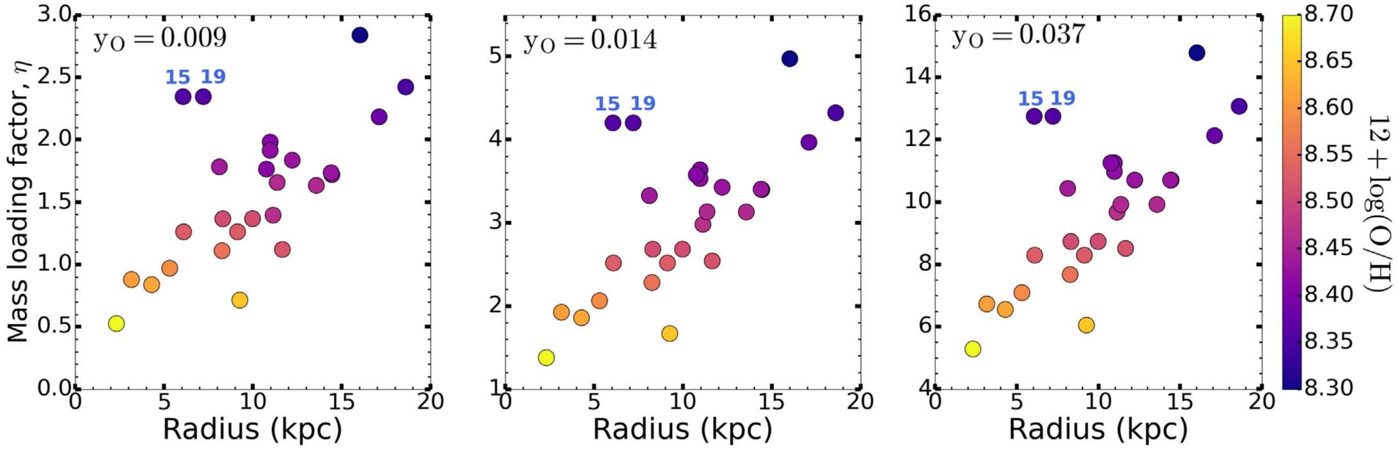

Figure 11. The mass loading factor η, modeled using Equation (7), of 26 H II regions as a function of galactocentric radius assuming $y_O = 0.009$ (left), $y_O = 0.014$ (middle), and $y_O = 0.037$ (right). The points are color coded by their gas-phase metallicity. The mass loading factor, as represented in the chemical analysis, gets impacted by metal dilution from low-metallicity gas accretion if $\dot{M}_{\rm inflow} = \dot{M}_\star$ and thus deviates from the traditional definition.

how using this model would affect the effective yields of the H II regions and found that $y_{\rm eff} < y_O$, which suggests that accretion cannot be the only mechanism occurring.

Chemical evolution models that include both inflows and outflows may offer a more realistic model to describe galaxies like NGC 99. J. Bovy (2023, in preparation) provides an adjusted form of the accreting box known as the "gas regulatory" or "bathtub" model, which includes outflows (B. M. Tinsley 1973; B. M. Tinsley & R. B. Larson 1978; N. Bouché et al. 2010; S. J. Lilly et al. 2013). In this model, it is assumed that the star formation rate is equal to the inflow rate ($\dot{M}_{\rm inflow}$) of material or $\dot{M}_\star = \dot{M}_{\rm inflow}$, which has been found to be broadly correct on global scales based on simulations and modeling (K. Finlator & R. Dave 2008; N. Bouché et al. 2010; P. Dayal et al. 2013; Y.-j. Peng & R. Maiolino 2014). The model can be described by the equation

$$Z_{\rm gas} = \frac{y}{1+\eta}\left\{1 - \exp\left([1+\eta]\left[1 - \frac{1}{f_{\rm gas}}\right]\right)\right\}, \qquad (7)$$

where the mass loading factor, η, is defined as $\eta = \dot{M}_{\rm outflow}/\dot{M}_\star$. Setting $y = y_O$, we solve Equation (7) for η to see how the mass loading factor varies as a function of galactocentric radius. We find that most of the H II regions show a higher mass loading factor at a higher galactocentric radius, except for two of them, as seen in Figure 11. For their given radius, the two ALM H II regions (regions 15 and 19) both show a high η for their respective position in the galaxy.

Figure 11 shows that η can vary from 0.5–15 depending on the value of y_O. Mass loading factors of this scale are typically found in starbursting galaxies (T. M. Heckman et al. 2015). Following G. Rodighiero et al. (2011), a galaxy is defined to be starbursting if $\mathrm{SFR_{global}/SFR_{MS}} > 4$, where $\mathrm{SFR_{MS}}$ is the global SFR from the star-forming galaxy main sequence (MS). We utilize the time-dependent MS equation of J. S. Speagle et al. (2014) to determine $\mathrm{SFR_{MS}} = 1.64\,M_\odot\,\mathrm{yr}^{-1}$. Therefore, $\mathrm{SFR_{global}/SFR_{MS}} = 1.74$, so NGC 99 is not currently in a starbursting phase. For cases where η is much greater than 1, the mass loading factor becomes nonphysical for a galaxy of this mass (J. Chisholm et al. 2017; X. Xu et al. 2022).

Therefore, the most likely value of true yield is around $y_{\rm O} = 0.009$. Regardless of $y_{\rm O}$, a correlation between η and R is evident. η increases with radius and shows an inverse correlation with stellar density. The mass loading factor is highest in the outermost H II regions, which is contradictory to the traditional expectation for η. Instead, the high mass loading factors are an artifact of the model we assumed. Equation (7) shows that η and $Z_{\rm gas}$ are roughly inversely related; therefore, a lower metallicity can result in higher mass loading factor values. The color coding in Figure 11 confirms that η has an inverse relation with gas-phase metallicity. The outer H II regions with lower metallicities have the highest mass loading factors. This suggests that η, in this situation, is tracing gas dilution due to inflow.

Both processes, the outflow of metal-rich gas and inflow of low-metallicity gas accretion, can lower the metallicity of the H II regions, causing their mass loading factor to be high. Even if NGC 99 had an outflow (which we cannot be certain about), it would have η proportional to the star formation rate, which can be approximated by the stellar mass surface density today if a significant fraction of the stellar mass was created in that burst. Since that is not the case, the most likely process leading to the increasing η trend with radius would be the accretion of lower metallicity gas. This is supported by the fact that gas accretion is believed to occur mostly at the outskirts of the galactic disks along their major axis (C. Peroux et al. 2020).

We acknowledge that the bathtub chemical evolution models are not sophisticated enough to precisely model the processes of mixing and diffusion. Another limitation of the model is that it does not account for differential accretion, i.e., when $\dot{M}_\star \neq \dot{M}_{\rm inflow}$ and $\dot{M}_{\rm inflow}$ is independent of $\dot{M}_\star$. Nevertheless, this model helps us understand the balance of gas outflow and inflow in a qualitative manner, which is what we advise the reader to take away from this discussion.

4.3. Estimation of Accreted Mass

We can estimate the accreted amount of low-metallicity gas needed to dilute the original gas present in the two ALM regions to the metallicity value we observe today. The accreted mass $M_{\rm H,acc}$ can be given by the following equation

$$M_{\rm H,acc} = M_{\rm H,now} - M_{\rm H,orignal}, \quad (8)$$

where $M_{\rm H,now}$ is the hydrogen mass of the region now, and $M_{\rm H,original}$ is the original hydrogen mass of the system. We assume that the metals in the H II regions are primarily made up of oxygen, so the mass in metals we currently see $M_{\rm O,now}$ can then be given by

$$M_{\rm O,now} = M_{\rm O,original} + M_{\rm O,acc}, \quad (9)$$

where $M_{\rm O,original}$ is the original oxygen mass of the region before dilution and $M_{\rm O,acc}$ is the oxygen mass that was accreted in. If we assume that the gas accreted was pristine, that is $M_{\rm O,acc} = 0$, then $M_{\rm O,now} = M_{\rm O,original}$. The oxygen mass can then be estimated using metallicity and H I 21 cm mass values using $M_{\rm O,now} = M_{\rm Hnow,} \times Z_{\rm now,ALM}$ where $Z_{\rm now,ALM}$ is the measured metallicity of the two ALM regions. We convert $12 + \log({\rm O/H})$ to $Z_{\rm now,ALM}$ using Equation (5). We estimate the mass of oxygen originally present in regions 15 and 19 to be $8.8 \times 10^3\,M_\odot$ and $8.2 \times 10^3\,M_\odot$, respectively. The original amount of hydrogen is $M_{\rm H,original,} = M_{\rm O,original}/Z_{\rm original}$ where $Z_{\rm original}$ is the metallicity of the H II regions before dilution. $Z_{\rm original}$ is estimated using the linear fitted metallicity gradient from the N2 indicator , where we excluded the ALM regions from the fit, which can be found in Table A2. $Z_{\rm original}$ for the two regions is 8.57 and 8.55. Thus, $M_{\rm H,original}$ of the H II regions is $2.01 \times 10^6\,M_\odot$ and $1.98 \times 10^6\,M_\odot$. Using Equation (8), we estimate the accreted hydrogen mass needed to dilute the systems to be $1.26 \times 10^6\,M_\odot$ and $1.08 \times 10^6\,M_\odot$ for regions 15 and 19, respectively.

These accreted masses should be considered lower limits since we assume that the accreted gas is pristine. The masses of the accreted gas clouds are similar to those found in high-velocity clouds (HVC) around the Milky Way (M. E. Putman et al. 2012).

4.4. CGM of NGC 99

The absorption spectra at the position of the QSO J0023+1547 trace four clouds in Lyα, the strongest of which matches the velocity of the H I 21 cm emitting ISM within the disk of the NGC 99. Figure 12 shows the ISM kinematics as traced by H I 21 cm with the galaxy's optical map overlaid. The position of the QSO is indicated with a filled circle that is color coded to the velocity of the strongest component (A). The strongest component (see Table 2) is corotating with the ISM with an uncertainty of less than 5 km s^{-1}. The large synthesized beam ($50''\!.5 \times 47''\!.5$) of the VLA smears the small-scale velocity structure of the H I data. Therefore, the precise measurement of velocity at the edge of the H I disk is not possible with our data.

The corotating component has a column density, $N({\rm H\,I}) \geqslant 10^{14.4}$ cm^{-2}, which is more than an order of magnitude higher than all the other three components put together, indicating that most of the neutral material is corotating. The three weaker components are noncorotating, i.e., their velocities are reversed from what is seen on the blueshifted side of the galaxy. If the covering fraction of the strong component is large, then we are looking at the extended disk material associated with the disk. Galaxy simulations have seen the presence of large extended corotating disks (K. R. Stewart et al. 2011). Recent simulations by Z. Hafen et al. (2022) also found that gas accreting into thin-disk galaxies in the FIRE simulations is dominated by rotating cooling flows. The hotter accreting gas cools down to 10^4 K, and its geometry transitions from a quasi-spherical distribution to a cool extended disk.

The CGM gas distributions and kinematics suggest two possible entryways for gas into the disk of the galaxies. First is through the extended disk traced by the dominant component. While the gas in the extended disk is much further from where the ALMs are seen (at galactocentric radii of <10 kpc), the gas may flow inward without much metal mixing for galaxies with low gas dispersion ($\sigma_g \sim 14$ km s^{-1}) through radial flows in the ISM (P. Sharda et al. 2021). The steep increase in the mass loading fraction as a function of radius (see Figure 11) suggests that gas dilution via accretion is increasingly important at large radii. This scenario is consistent with the radial flow of low-metallicity gas along the disk. M. Padave et al. (2024a) find no correlation between the neutral gas content of the CGM and inside-out disk growth, suggesting that gas likely transverses large distances to get to the inner stellar disk before forming stars.

The second pathway is through the halo vertically to the disk. HVCs are one such example that shows an overall infall

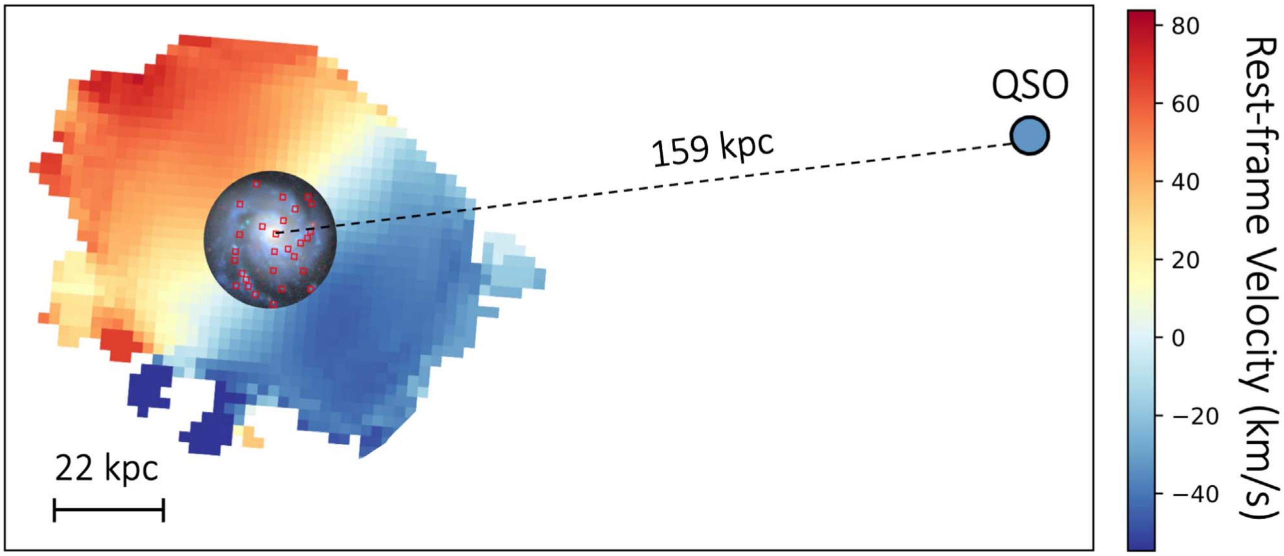

Figure 12. An optical image of NGC 99 overlaid with VLA H I 21 cm map showing extended H I emission beyond the optical disk of the galaxy. The spatial location of QSO (J0023+1547) is shown relative to NGC 99, with the color of the point corresponding to the velocity centroid of the dominant component of the Lyα line. The primary component of the CGM is corotating at roughly the same velocity as the ISM closest to the sightline. This suggests a large disk extending out to the CGM.

that is believed to support star formation in the Milky Way (N. Lehner et al. 2022). Our estimate of the inflowing cloud masses needed to produce the ALMs falls within the HVC mass range of the Milky Way (M. E. Putman et al. 2012) and anomalous velocity clouds analogous to intermediate-velocity clouds seen in NGC 4321 (Gim et al. 2021).

No metal absorbers associated with the hydrogen clouds were detected (Table 2). This is not surprising as even at solar metallicity, the metal lines are expected to be very weak for gas clouds of $N(\mathrm{H\,I}) \geqslant 10^{14-15}\ \mathrm{cm}^{-2}$. We do not expect the Lyα absorbers to be tracing highly ionized gas as we did not detect high-ionization species such as Si IV and N V.

4.5. Fundamental Metallicity Relation on Resolved Scales

J. Lequeux et al. (1979), D. Zaritsky et al. (1994), and C. A. Tremonti et al. (2004) established a positive correlation between global metallicity and the $M_\star$ of galaxies, known as the mass–metallicity relation (MZR). Modern studies, such as MaNGA, have shown that the MZR evolves over cosmic time (K. Bundy et al. 2015; A. Camps-Fariña et al. 2022). In addition, observations have shown that metallicity and $M_\star$ depend on SFR (M. A. Lara-López et al. 2010; F. Mannucci et al. 2010; M. Curti et al. 2020). The relation between the three properties is known as the FMR. M. A. Lara-López et al. (2010) and F. Mannucci et al. (2010) found that at a fixed $M_\star$, a higher SFR yields a lower metallicity. Additionally, as $M_\star$ increases, so do metallicity and SFR. Results from F. F. Rosales-Ortega et al. (2012), which were later confirmed by J. K. Barrera-Ballesteros et al. (2016), established that the MZR and FMR also occur on localized (subkiloparsec) scales. We will further explore the FMR here.

We derived the SFR from the Hα emission line using

$$\log \mathrm{SFR}(M_\odot\ \mathrm{yr}^{-1}) = \log L_x - \log C_x \tag{10}$$

where $\log C_x = 41.27$ and L_x, in units of erg s^{-1}, is the Hα luminosity derived from the integrated and dust-corrected Hα flux at a distance of 79.4 Mpc (C.-N. Hao et al. 2011; E. J. Murphy et al. 2011; R. C. Kennicutt & N. J. Evans 2012). We convert $M_\star$ and SFR to stellar mass surface density ($\Sigma_\star$) and star formation rate surface density (Σ_{SFR}), respectively, by dividing $M_\star$ and SFR by the area of each slit, 0.35 kpc^2.

We investigate the relationship between $\Sigma_\star$, Σ_{SFR}, and metallicity by plotting the data in 3D space to gain a better visual representation. Figure 13 shows the $\Sigma_\star$, Σ_{SFR}, and $12 + \log(\mathrm{O/H})$ parameter space with the filled circles color coded based on their galactocentric radius in kpc. We fit a plane to the data and find that the relationship between the three properties is described by the equation:

$$\begin{aligned} 12 + \log(\mathrm{O/H}) = {} & (-0.144 \pm 0.044) \times \log(\Sigma_{\mathrm{SFR}}) \\ & + (0.225 \pm 0.050) \times \log(\Sigma_\star) \\ & + (6.443 \pm 0.455). \end{aligned} \tag{11}$$

Figure 13 is available as an online video where we rotate about the z-axis one time so that the entirety of the plane is seen. The coefficients in front of the two surface density parameters describe how and to what strength gas-phase metallicity depends on local $\Sigma_\star$ and Σ_{SFR}. The resolved FMR (rFMR), given by Equation (11), shows that for a given $\Sigma_\star$, metallicity relates inversely with Σ_{SFR}. Moreover, for a given Σ_{SFR}, metallicity depends proportionally on $\Sigma_\star$. The value of the coefficients, −0.144 and 0.225, for Σ_{SFR} and $\Sigma_\star$, respectively, reveals that the metallicity of the H II regions has a stronger dependence on $\Sigma_\star$ than Σ_{SFR}. The scatter in metallicity around the best-fit plane is $\sigma_{\mathrm{FMR}} = 0.07$ dex, which is comparable to the scatter of the surface fit by M. Curti et al. (2020). W. M. Baker et al. (2023) recently found similar results using 56,000 H II regions from the MaNGA survey and measure $\sigma_{\mathrm{FMR}} = 0.06$ dex.

Our rFMR equation presents the resolved FMR at spatial scales of 4″ (1.5 kpc), which provides a view of kpc scale physics that may be responsible for the observed relationship. The spatial resolution we achieve is comparable to some of the IFU surveys; however, the multiobject spectrograph allows us to sample a much larger region of the galaxy going well beyond

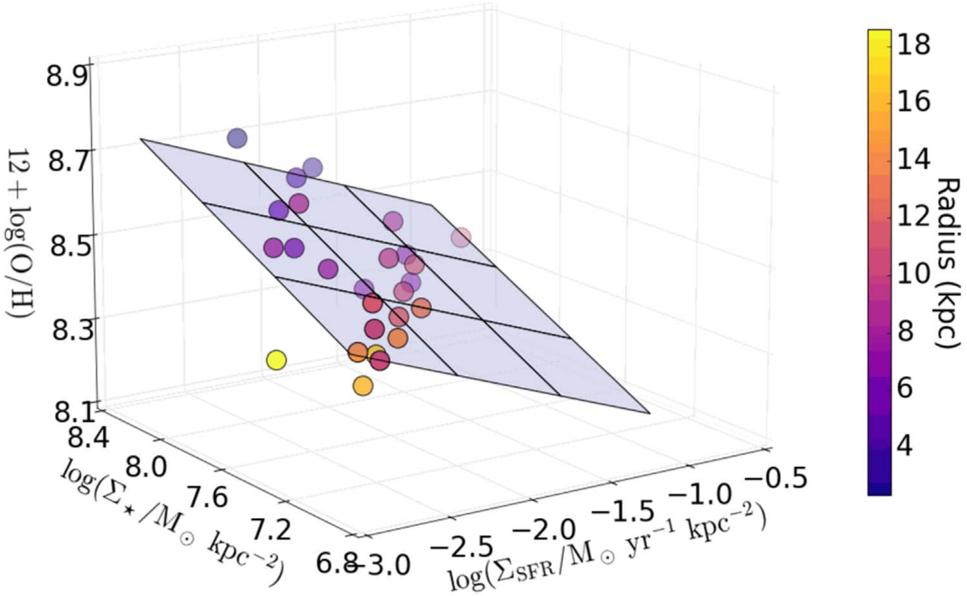

Figure 13. 3D visualization of the resolved Fundamental Metallicity Relation for the 26 H II regions in the galaxy NGC 99 color coded by galactocentric radius. The *x*-axis and *y*-axis are the stellar mass and star formation rate surface densities, respectively, for each region. Gas-phase metallicities from the N2 indicator are shown on the *z*-axis. The points are well fit my a linear plane described by Equation (11). An animated version of this figure is available online, where we rotate around the *z*-axis for one full rotation in an 18 s animation.

(An animation of this figure is available in the online article.)

R_{25}. Moreover, the size of our Binospec slits encompasses the gas and stars within the observed regions allowing us to probe their chemical characteristics. Studies on the rFMR have been done using spatially resolved data from the MaNGA sample, which samples spatial scales of about 1.5 kpc (J. K. Barrera-Ballesteros et al. 2016; L. Sánchez-Menguiano et al. 2019; B. B. Teklu et al. 2020). We will increase our sample size and spatial resolution in a future study.

5. Summary

In this pilot study, we study the properties of 26 H II regions in the galaxy NGC 99. We measured the radial metallicity gradient from strong-line metallicity indicators of N2 and O3N2 to investigate indirect evidence of gas accretion. Additionally, we analyze the chemical evolution of the systems by assuming a closed-box, accreting box, and accreting/outflow box models. We measure an effective yield and mass loading factor for each region. Finally, we derive a resolved Fundamental Metallicity Relation by connecting the metallicity information to $\Sigma_\star$ and $\Sigma_{\rm SFR}$. The results are summarized below:

1. Using oxygen gas-phase metallicities calibrated using the N2 metallicity index, we measure the radial metallicity gradient of NGC 99 to be -0.017 dex kpc^{-1} or, in terms of R_{25}, -0.19 dex$/R_{25}$. Our radial gradient matches with the peak of the distribution of radial gradients found by other studies (D. A. Berg et al. 2020; L. S. Pilyugin et al. 2023).
2. We discover two anomalously low-metallicity regions with a high difference between the H I and Hα gas line-of-sight velocities. We believe that these two regions are an indirect sign of the accretion of low-metallicity gas from the CGM that diluted the gas used to form the stars in these regions.
3. Assuming the closed-box model, we find that the effective yield of each observed H II region is below the true nucleosynthetic yield. Additionally, the effective yields are roughly constant with a galactocentric radius. These results lead us to believe that the galaxy has a varying degree of inflows and outflows.
4. When inflow and outflows are incorporated, we find that the H II regions have a mass loading factor between 0.5 and 15, depending on the choice of $y_{\rm O}$. Additionally, we suggest higher accretion rates of low-metallicity gas in the outskirts of the galaxy as the reason for higher η values at higher radii. This occurs as a consequence of using the bathtub model, which does not account for differential accretion.
5. We find Lyα absorbers associated with the CGM of the galaxy at an impact parameter 159 kpc. The strongest component of the absorption feature kinematically matches the disk kinematics closest to the sightline. This may hint at the presence of an extended disk, assuming that the covering fraction of the absorbing media is high. We suggest that a large H I disk may be a possible pathway for low-metallicity gas to flow into the ISM of this galaxy.
6. We derive Equation (11) describing the resolved Fundamental Metallicity Relation relating Z, $\Sigma_\star$, and $\Sigma_{\rm SFR}$. We find that for a given $\Sigma_\star$, $\Sigma_{\rm SFR}$ increases with decreasing metallicity. From this result, we believe that the local physics within galaxies affects the global scale physics. Our equation is useful for estimating metallicities in galaxies where only imaging data might be available, which is especially the case for higher redshift galaxies.

Future work will expand this analysis to other galaxies in the DIISC sample to look for other ALM H II regions and grow our sample size for the rFMR to improve the precision of the plane. Multiwavelength studies of local galaxies are critical to obtaining a detailed look into how galaxies obtain their gas and how it is processed for star formation.

Acknowledgments

We thank Jackie Monkiewicz, Ben Weiner, Chris Howk, Mirko Curti, and Patrick Kamieneski for the valuable and useful discussions during the course of this work. We thank the referee for constructive comments. We thank the support staff at the MMT Observatory, the Steward Observatory, the Vatican Advanced Technology Telescope, the Very Large Array, the National Radio Astronomy Observatory, and the Space Telescope Science Institute for help with this project. All HST data presented in this paper were obtained from the Mikulski Archive for Space Telescopes (MAST) at the Space Telescope Science Institute. The specific observations analyzed can be accessed via doi:10.17909/rf6m-3y73.

The Arizona State University authors acknowledge the 23 Native Nations that have inhabited this land for centuries. Arizona State University's four campuses are located in the Salt River Valley on ancestral territories of Indigenous peoples, including the Akimel O'odham (Pima) and Pee Posh (Maricopa) Indian Communities, whose care and keeping of these lands allows us to be here today.

This material is based upon work supported by the National Science Foundation Graduate Research Fellowship Program under grant No. 2233001. Any opinions, findings, and conclusions or recommendations expressed in this material are those of the author(s) and do not necessarily reflect the views of the National Science Foundation.

A.O., S.B., M.P., B.K., H.G., and C.D. are supported by the NSF grants 2108159 and 2009409. M.P., S.B., and R.J. are supported by NASA ADAP grant 80NSSC21K0643. S.B., H.G., and T.H. are also supported by Hubble Space Telescope (HST) grant HST-GO-14071 administrated by STScI, operated by AURA under contract NAS 5-26555 from NASA.

Observations reported here were obtained at the MMT Observatory, a joint facility of the Smithsonian Institution and the University of Arizona.

This work is also partly based on observations with the VATT: the Alice P. Lennon Telescope and the Thomas J. Bannan Astrophysics Facility.

The National Radio Astronomy Observatory is a facility of the National Science Foundation operated under a cooperative agreement by Associated Universities, Inc.

Facility: HST, GALEX, MMT (Binospec), VATT and VLA.

Software: astropy (Astropy Collaboration et al. 2013, 2018, 2022), CASA (J. P. McMullin et al. 2007), `ipython/jupyter` (F. Perez & B. E. Granger 2007; T. Kluyver et al. 2016), `matplotlib` (J. D. Hunter 2007), `NumPy` (C. R. Harris et al. 2020), `pyFIT3D` (E. A. D. Lacerda et al. 2022), `SoFiA-2` (P. Serra et al. 2015; T. Westmeier et al. 2021), `statmorph` (V. Rodriguez-Gomez et al. 2019), `specutils` (N. Earl et al. 2022), and `Python` from https://www.python.org.

Appendix

The Appendix section contains tables that were referenced to in the main text. Table A1 contains the position of each H II region as well as the measured properties of the regions such as Hα flux, Balmer decrement, metallicity indicator values, and gas velocities. In addition, Table A2 contains the fitted line

Table A1

NGC 99 H II Region Position, Flux, Balmer, and Metallicity Indicator Values

H II Region	R.A. (deg)	Decl. (deg)	Radius (kpc)	F(Hα) (erg s^{-1} cm^{-2})	F(Hα)/F(Hβ)	N2	O3N2	S2	$V_{\mathrm{H}\alpha}$ (km s^{-1})	$V_{\mathrm{H\,I}}$ (km s^{-1})
1	5.9966	15.7598	14.4	1.27	4.44 ± 0.41	−0.966 ± 0.127	1.2726 ± 0.1349	−0.699 ± 0.051	−66.33	−26.41
2	5.9907	15.7627	14.4	2.56	3.37 ± 0.31	−0.974 ± 0.098	1.4556 ± 0.1050	−0.651 ± 0.067	−23.78	−35.86
3	5.9952	15.7621	11.7	1.71	3.19 ± 0.14	−0.802 ± 0.048	0.8396 ± 0.0580	−0.611 ± 0.043	−39.04	−29.07
4	6.0006	15.7620	12.2	4.26	3.98 ± 0.38	−0.975 ± 0.069	1.5007 ± 0.0815	−0.658 ± 0.043	−17.45	−13.18
5	6.0026	15.7620	13.6	4.73	3.65 ± 0.16	−0.919 ± 0.024	1.3667 ± 0.0352	−0.668 ± 0.020	−3.44	−3.20
6	6.0009	15.7628	11.4	13.13	3.81 ± 0.17	−0.917 ± 0.025	1.2389 ± 0.0373	−0.740 ± 0.025	−10.99	−3.98
7	6.0014	15.7634	11.0	79.82	5.14 ± 0.15	−1.006 ± 0.017	1.4924 ± 0.0265	−0.913 ± 0.016	−33.62	−3.98
8	5.9934	15.7662	8.3	2.79	4.29 ± 0.21	−0.823 ± 0.035	0.9739 ± 0.0482	−0.537 ± 0.029	−47.36	−25.09
9	5.9976	15.7658	6.1	2.67	4.45 ± 0.28	−0.776 ± 0.039	0.8317 ± 0.0530	−0.658 ± 0.456	−28.33	−7.96
10	6.0032	15.7662	10.0	6.72	4.17 ± 0.10	−0.826 ± 0.021	1.0075 ± 0.0250	−0.737 ± 0.019	23.09	10.26
11	6.0033	15.7678	9.1	14.58	3.80 ± 0.23	−0.778 ± 0.025	0.9274 ± 0.0429	−0.705 ± 0.024	48.38	14.89
12	5.9945	15.7682	5.3	2.96	4.13 ± 0.28	−0.658 ± 0.034	0.2986 ± 0.0581	−0.625 ± 0.037	−30.18	−16.45
13	5.9952	15.7684	4.3	5.90	4.16 ± 0.22	−0.610 ± 0.020	0.1732 ± 0.0420	−0.725 ± 0.025	−30.31	−16.45
14	5.9977	15.7686	2.3	3.52	3.90 ± 0.19	−0.470 ± 0.026	0.1633 ± 0.0397	−0.570 ± 0.030	−6.32	−3.24
15	5.9935	15.7696	6.1	12.79	4.39 ± 0.42	−1.104 ± 0.059	1.3145 ± 0.0749	−0.940 ± 0.068	−66.76	−17.18
16	5.9922	15.7714	8.1	19.80	4.46 ± 0.10	−0.954 ± 0.019	1.3544 ± 0.0261	−0.725 ± 0.016	−50.78	−16.78
17	5.9994	15.7716	3.2	10.49	4.34 ± 0.14	−0.629 ± 0.024	0.2426 ± 0.0356	−0.661 ± 0.024	38.13	13.55
18	5.9920	15.7753	10.8	1.60	3.60 ± 0.24	−1.018 ± 0.042	1.4242 ± 0.0565	−0.562 ± 0.088	15.93	−6.40
19	5.9946	15.7744	7.2	24.62	4.23 ± 0.19	−1.107 ± 0.027	1.5927 ± 0.0338	−0.956 ± 0.024	−35.09	3.64
20	6.0028	15.7742	9.3	2.12	4.44 ± 0.41	−0.560 ± 0.026	0.6094 ± 0.0555	−0.414 ± 0.019	41.59	32.41
21	5.9926	15.7763	11.1	1.64	3.88 ± 0.30	−0.898 ± 0.054	0.9573 ± 0.0772	−0.533 ± 0.046	−1.43	2.89
22	5.9980	15.7763	8.3	1.56	3.90 ± 0.30	−0.727 ± 0.038	0.9263 ± 0.0517	−0.546 ± 0.037	73.33	21.22
23	6.0008	15.7776	11.0	9.27	4.25 ± 0.14	−0.998 ± 0.016	1.4131 ± 0.0227	−0.801 ± 0.018	32.00	30.57
24	6.0007	15.7816	16.0	2.37	4.12 ± 0.19	−1.212 ± 0.052	1.7082 ± 0.0563	−0.842 ± 0.035	34.68	37.89
25	6.0020	15.7819	17.1	2.40	3.85 ± 0.16	−1.070 ± 0.033	1.2779 ± 0.0429	−0.638 ± 0.023	55.76	42.14
26	6.0034	15.7825	18.6	1.09	3.97 ± 0.20	−1.12 ± 0.085	1.6681 ± 0.0901	−0.638 ± 0.038	48.44	47.21

Note. Flux is in units of $\times 10^{-16}$ erg s^{-1} cm^{-2}.

Table A2
Metallicity Radial Gradients

y	x	Slope m	Intercept b	Comment	Spearman ρ
N2	R	-0.032 ± 0.007	-0.564 ± 0.073		
$12 + \log(O/H)_{N2}$	R	-0.017 ± 0.004	8.646 ± 0.038		-0.60
$12 + \log(O/H)_{N2}$	R	-0.020 ± 0.003	8.693 ± 0.029	ALMs removed	-0.80
$12 + \log(O/H)_{N2}$	R/R_{25}	-0.191 ± 0.041	8.644 ± 0.038		
O3N2	R	0.083 ± 0.015	0.249 ± 0.166		
$12 + \log(O/H)_{O3N2}$	R	-0.020 ± 0.004	8.703 ± 0.041		-0.63
$12 + \log(O/H)_{O3N2}$	R	-0.023 ± 0.003	8.746 ± 0.035	ALMs removed	-0.77

Note. Linear fit equations to the metallicity vs. galactocentric radius data. Slopes are all in dex kpc^{-1} except for when $x = R/R_{25}$ which gives slope units of dex R_{25}^{-1}. Intercepts are all in dex.

Table A3
Properties of SDSS J002353.17+154356.8

Parameter	Value
R.A.[a] (α_{2000})	$00^h23^m53\overset{s}{.}17$
Decl.[a] (δ_{2000})	$+15°43'56\overset{''}{.}87$
Redshift	0.01747
Projected distance to NGC 99	57 kpc
Velocity offset to NGC 99 ($\Delta V_{H\alpha}$)	-74.51 km s^{-1}
Stellar mass[b]	$8.62 \times 10^8 M_\odot$
H I mass[c]	$5.8 \times 10^9 M_\odot$
N2	-0.46
$12 + \log(O/H)$	8.71

Notes.

[a] M. F. Skrutskie et al. (2006).

[b] M. Padave et al. (2024a).

[c] H. B. Gim et al. 2024, in preparation.

Table A4
Calculated Physical Properties of H II Regions

H II Region	Radius (kpc)	$12 + \log(\mathrm{O/H})_{\mathrm{N2}}$	$12 + \log(\mathrm{O/H})_{\mathrm{O3N2}}$	$\log(\Sigma_{\mathrm{SFR}})$ ($M_\odot$ yr^{-1} kpc^{-2})	$\log(\Sigma_\star)$ ($M_\odot$ kpc^{-2})	$\log(M_{\mathrm{HI}})$ ($M_\odot$)	f_{gas}	$\log(y_{\mathrm{eff}})$	η for $y_{\mathrm{O}} = 0.009$	η for $y_{\mathrm{O}} = 0.014$	η for $y_{\mathrm{O}} = 0.037$
1	14.4	8.43 ± 0.07	8.456 ± 0.036	−2.79	7.02	6.38	0.47	−2.38	1.72	3.40	10.70
2	14.4	8.43 ± 0.05	8.405 ± 0.030	−2.49	7.09	6.43	0.46	−2.39	1.73	3.40	10.70
3	11.7	8.52 ± 0.03	8.565 ± 0.014	−2.64	7.08	6.43	0.46	−2.30	1.83	2.54	8.51
4	12.2	8.43 ± 0.04	8.392 ± 0.024	−2.26	7.29	6.42	0.34	−2.53	1.98	3.43	10.70
5	13.6	8.46 ± 0.01	8.430 ± 0.010	−2.21	7.21	6.37	0.36	−2.48	1.26	3.13	9.92
6	11.4	8.46 ± 0.01	8.465 ± 0.010	−1.77	7.68	6.45	0.19	−2.69	2.34	3.13	9.92
7	11.0	8.41 ± 0.01	8.394 ± 0.008	−0.99	8.12	6.45	0.08	−2.93	1.78	3.64	11.25
8	8.3	8.51 ± 0.02	8.533 ± 0.012	−2.43	7.56	6.51	0.25	−2.56	0.88	2.68	8.73
9	6.1	8.53 ± 0.02	8.567 ± 0.013	−2.44	7.75	6.53	0.19	−2.63	2.34	2.52	8.29
10	10.0	8.51 ± 0.02	8.525 ± 0.007	−2.05	7.56	6.48	0.24	−2.57	1.39	2.68	8.73
11	9.1	8.53 ± 0.01	8.544 ± 0.011	−1.71	7.87	6.49	0.14	−2.70	1.91	2.52	8.29
12	5.3	8.59 ± 0.02	8.686 ± 0.012	−2.38	7.92	6.53	0.14	−2.64	2.84	2.06	7.09
13	4.3	8.62 ± 0.01	8.712 ± 0.009	−2.07	8.12	6.53	0.09	−2.69	2.42	1.86	6.55
14	2.3	8.70 ± 0.02	8.714 ± 0.009	−2.26	8.31	6.54	0.20	−2.44	2.18	1.38	5.28
15	6.1	8.36 ± 0.03	8.444 ± 0.021	−1.80	7.96	6.51	0.12	−2.90	1.76	4.20	12.75
16	8.1	8.44 ± 0.01	8.433 ± 0.008	−1.59	7.89	6.48	0.13	−2.80	0.97	3.33	10.43
17	3.2	8.61 ± 0.02	8.698 ± 0.007	−1.82	8.26	6.52	0.22	−2.51	1.36	1.92	6.73
18	10.8	8.41 ± 0.02	8.414 ± 0.017	−2.69	6.99	6.43	0.51	−2.34	1.26	3.58	11.25
19	7.2	8.36 ± 0.02	8.364 ± 0.010	−1.51	7.94	6.49	0.12	−2.90	1.12	4.20	12.75
20	9.3	8.65 ± 0.02	8.619 ± 0.013	−2.51	7.66	6.46	0.19	−2.50	1.66	1.67	6.05
21	11.1	8.47 ± 0.03	8.537 ± 0.019	−2.67	7.04	6.43	0.48	−2.32	0.84	2.98	9.67
22	8.3	8.56 ± 0.02	8.544 ± 0.013	−2.67	7.65	6.47	0.20	−2.57	1.37	2.28	7.67
23	11.0	8.42 ± 0.01	8.417 ± 0.007	−1.93	7.59	6.44	0.21	−2.70	1.11	3.53	10.97
24	16.0	8.30 ± 0.03	8.328 ± 0.018	−2.54	7.24	6.35	0.33	−2.68	0.71	4.97	14.78
25	17.1	8.38 ± 0.02	8.454 ± 0.012	−2.52	7.18	6.34	0.36	−2.56	0.52	3.97	12.13
26	18.6	8.35 ± 0.05	8.341 ± 0.029	−2.87	7.44	6.28	0.21	−2.77	1.63	4.32	13.07

parameters from Figure 5 while Table A3 shows the basic properties of NGC 99's companion SDSS J002353.17 +154356.8. Table A4 consists of the calculated properties of the H II regions such as gas-phase metallicity, stellar mass surface density, and SFR surface density.

ORCID iDs

Alejandro J. Olvera https://orcid.org/0000-0002-2819-0753
Sanchayeeta Borthakur https://orcid.org/0000-0002-2724-8298
Mansi Padave https://orcid.org/0000-0002-3472-0490
Timothy Heckman https://orcid.org/0000-0001-6670-6370
Hansung B. Gim https://orcid.org/0000-0003-1436-7658
Brad Koplitz https://orcid.org/0000-0001-5530-2872
Christopher Dupuis https://orcid.org/0000-0003-1739-3640
Emmanuel Momjian https://orcid.org/0000-0003-3168-5922
Rolf A. Jansen https://orcid.org/0000-0003-1268-5230

References

Acharyya, A., Krumholz, M. R., Federrath, C., et al. 2020, MNRAS, 495, 3819
Aihara, H., Allende Prieto, C., An, D., et al. 2011, ApJS, 193, 29
Alloin, D., Collin-Souffrin, S., Joly, M., & Vigroux, L. 1979, A&A, 78, 200
Asplund, M., Amarsi, A. M., & Grevesse, N. 2021, A&A, 653, A141
Astropy Collaboration, Price-Whelan, A. M., Lim, P. L., et al. 2022, ApJ, 935, 167
Astropy Collaboration, Price-Whelan, A. M., Sipőcz, B. M., et al. 2018, AJ, 156, 123
Astropy Collaboration, Robitaille, T. P., Tollerud, E. J., et al. 2013, A&A, 558, A33
Baker, W. M., Maiolino, R., Belfiore, F., et al. 2023, MNRAS, 519, 1149
Barrera-Ballesteros, J. K., Heckman, T., Sánchez, S. F., et al. 2018, ApJ, 852, 74
Barrera-Ballesteros, J. K., Heckman, T. M., Zhu, G. B., et al. 2016, MNRAS, 463, 2513
Belfiore, F., Maiolino, R., & Bothwell, M. 2016, MNRAS, 455, 1218
Belfiore, F., Maiolino, R., Tremonti, C., et al. 2017, MNRAS, 469, 151
Berg, D. A., Pogge, R. W., Skillman, E. D., et al. 2020, ApJ, 893, 96
Bertin, E., & Arnouts, S. 1996, A&AS, 117, 393
Besla, G. 2015, arXiv:1511.03346
Bian, F., Kewley, L. J., & Dopita, M. A. 2018, ApJ, 859, 175
Boardman, N. F., Zasowski, G., Newman, J. A., et al. 2021, MNRAS, 501, 948
Borthakur, S., Padave, M., Heckman, T., et al. 2024, arXiv:2409.12554
Bouché, N., Dekel, A., Genzel, R., et al. 2010, ApJ, 718, 1001
Bournaud, F., & Elmegreen, B. G. 2009, ApJL, 694, L158
Bundy, K., Bershady, M. A., Law, D. R., et al. 2015, ApJ, 798, 7
Buta, R. J. 2019, MNRAS, 488, 590
Camps-Fariña, A., Sánchez, S. F., Mejía-Narváez, A., et al. 2022, ApJ, 933, 44
Cedrés, B., & Cepa, J. 2002, A&A, 391, 809
Cedrés, B., Cepa, J., Bongiovanni, Á., et al. 2012, A&A, 545, A43
Chisholm, J., Tremonti, C. A., Leitherer, C., & Chen, Y. 2017, MNRAS, 469, 4831
Curti, M., Cresci, G., Mannucci, F., et al. 2017, MNRAS, 465, 1384
Curti, M., Mannucci, F., Cresci, G., & Maiolino, R. 2020, MNRAS, 491, 944
Dayal, P., Ferrara, A., & Dunlop, J. S. 2013, MNRAS, 430, 2891
Dekel, A., Birnboim, Y., Engel, G., et al. 2009, Natur, 457, 451
Denicoló, G., Terlevich, R., & Terlevich, E. 2002, MNRAS, 330, 69
Dey, A., Schlegel, D. J., Lang, D., et al. 2019, AJ, 157, 168
Dopita, M. A., Kewley, L. J., Sutherland, R. S., & Nicholls, D. C. 2016, Ap&SS, 361, 61
Earl, N., Tollerud, E., O'Steen, R., et al. 2022, astropy/specutils: v1.8.0, Zenodo, doi:10.5281/zenodo.7015214
Edmunds, M. G. 1990, MNRAS, 246, 678
Espinosa-Ponce, C., Sánchez, S. F., Morisset, C., et al. 2020, MNRAS, 494, 1622
Faucher-Giguère, C.-A., & Oh, S. P. 2023, ARA&A, 61, 131
Finlator, K., & Davé, R. 2008, MNRAS, 385, 2181
Fitzpatrick, E. L., & Spitzer, L. J. 1997, ApJ, 475, 623
Font, A. S., McCarthy, I. G., Crain, R. A., et al. 2011, MNRAS, 416, 2802
Gim, H. B., Borthakur, S., Momjian, E., et al. 2021, ApJ, 922, 69
Green, J. C., Froning, C. S., Osterman, S., et al. 2012, ApJ, 744, 60
Hafen, Z., Stern, J., Bullock, J., et al. 2022, MNRAS, 514, 5056
Hao, C.-N., Kennicutt, R. C., Johnson, B. D., et al. 2011, ApJ, 741, 124
Harris, C. R., Millman, K. J., van der Walt, S. J., et al. 2020, Natur, 585, 357
Heckman, T. M., Alexandroff, R. M., Borthakur, S., Overzier, R., & Leitherer, C. 2015, ApJ, 809, 147
Hopkins, P. F., Keres, D., Oñorbe, J., et al. 2014, MNRAS, 445, 581
Howk, J. C., Rueff, K. M., Lehner, N., et al. 2018a, ApJ, 856, 166
Howk, J. C., Rueff, K. M., Lehner, N., et al. 2018b, ApJ, 856, 167
Hunter, J. D. 2007, CSE, 9, 90
Hwang, H.-C., Barrera-Ballesteros, J. K., Heckman, T. M., et al. 2019, ApJ, 872, 144
Jiang, X.-J., Wang, Z., Gu, Q., Wang, J., & Zhang, Z.-Y. 2015, ApJ, 799, 92
Ju, M., Yin, J., Liu, R., et al. 2022, ApJ, 938, 96
Kansky, J., Chilingarian, I., Fabricant, D., et al. 2019, PASP, 131, 075005
Kennicutt, R. C., & Evans, N. J. 2012, ARA&A, 50, 531
Kennicutt, R. C. J. 1998, ApJ, 498, 541
Kennicutt, R. C. J., & Garnett, D. R. 1996, ApJ, 456, 504
Kereš, D., Katz, N., Weinberg, D. H., & Davé, R. 2005, MNRAS, 363, 2
Kewley, L. J., & Dopita, M. A. 2002, ApJS, 142, 35
Kluyver, T., Ragan-Kelley, B., Pérez, F., et al. 2016, in Positioning and Power in Academic Publishing: Players, Agents and Agendas, ed. F. Loizides & B. Schmidt (Amsterdam: IOS Press), 87
Kravtsov, A. V., Vikhlinin, A. A., & Meshcheryakov, A. V. 2018, AstL, 44, 8
Lacerda, E. A. D., Sánchez, S. F., Mejía-Narváez, A., et al. 2022, NewA, 97, 101895
Lackner, C. N., Cen, R., Ostriker, J. P., & Joung, M. R. 2012, MNRAS, 425, 641
Lagos, P., Scott, T. C., Nigoche-Netro, A., et al. 2018, MNRAS, 477, 392
Lara-López, M. A., Cepa, J., Bongiovanni, A., et al. 2010, A&A, 521, L53
Larson, R. B. 1976, MNRAS, 176, 31
Lehner, N., Howk, J. C., Marasco, A., & Fraternali, F. 2022, MNRAS, 513, 3228
Leitherer, C., Ekström, S., Meynet, G., et al. 2014, ApJS, 212, 14
Lequeux, J., Peimbert, M., Rayo, J. F., Serrano, A., & Torres-Peimbert, S. 1979, A&A, 80, 155
Li, Y., Bresolin, F., & Kennicutt, R. C. J. 2013, ApJ, 766, 17
Lilly, S. J., Carollo, C. M., Pipino, A., Renzini, A., & Peng, Y. 2013, ApJ, 772, 119
Luo, Y., Heckman, T., Hwang, H.-C., et al. 2021, ApJ, 908, 183
Maeder, A. 1992, A&A, 264, 105
Maiolino, R., & Mannucci, F. 2019, A&ARv, 27, 3
Mandelbaum, R., Wang, W., Zu, Y., et al. 2016, MNRAS, 457, 3200
Mannucci, F., Cresci, G., Maiolino, R., Marconi, A., & Gnerucci, A. 2010, MNRAS, 408, 2115
Marino, R. A., Rosales-Ortega, F. F., Sánchez, S. F., et al. 2013, A&A, 559, A114
Martin, D. C., Fanson, J., Schiminovich, D., et al. 2005, ApJL, 619, L1
Martin, P., & Belley, J. 1996, ApJ, 468, 598
Matteucci, F., & Francois, P. 1989, MNRAS, 239, 885
McMullin, J. P., Waters, B., Schiebel, D., Young, W., & Golap, K. 2007, in ASP Conf. Ser. 376, Astronomical Data Analysis Software and Systems XVI, ed. R. A. Shaw, F. Hill, & D. J. Bell (San Francisco, CA: ASP), 127
Moran, S. M., Heckman, T. M., Kauffmann, G., et al. 2012, ApJ, 745, 66
Morrissey, P., Conrow, T., Barlow, T. A., et al. 2007, ApJS, 173, 682
Murphy, E. J., Condon, J. J., Schinnerer, E., et al. 2011, ApJ, 737, 67
Nagao, T., Maiolino, R., & Marconi, A. 2006, A&A, 459, 85
Oey, M. S., & Kennicutt, R. C. J. 1993, ApJ, 411, 137
Osterman, S., Green, J., Froning, C., et al. 2011, Ap&SS, 335, 257
Pace, Z. J., Tremonti, C., Schaefer, A. L., et al. 2021, ApJ, 908, 165
Padave, M., Borthakur, S., Gim, H. B., et al. 2024a, ApJ, 960, 24
Padave, M., Borthakur, S., Jansen, R. A., et al. 2024b, arXiv:2407.16690
Parikh, T., Thomas, D., Maraston, C., et al. 2021, MNRAS, 502, 5508
Pellegrini, E. W., Oey, M. S., Winkler, P. F., et al. 2012, ApJ, 755, 40
Peng, Y.-j., & Maiolino, R. 2014, MNRAS, 443, 3643
Perez, F., & Granger, B. E. 2007, CSE, 9, 21
Peroux, C., Nelson, D., van de Voort, F., et al. 2020, MNRAS, 499, 2462
Pettini, M., & Pagel, B. E. J. 2004, MNRAS, 348, L59
Pezzulli, G., & Fraternali, F. 2016, MNRAS, 455, 2308
Pilyugin, L. S., Tautvaišienė, G., & Lara-López, M. A. 2023, A&A, 676, A57
Pogge, R. W., Atwood, B., Brewer, D. F., et al. 2010, Proc. SPIE, 7735, 77350A
Putman, M. E., Peek, J. E. G., & Joung, M. R. 2012, ARA&A, 50, 491
Rodighiero, G., Daddi, E., Baronchelli, I., et al. 2011, ApJL, 739, L40
Rodriguez-Gomez, V., Snyder, G. F., Lotz, J. M., et al. 2019, MNRAS, 483, 4140

Rosales-Ortega, F. F., Diaz, A. I., Kennicutt, R. C., & Sanchez, S. F. 2011, MNRAS, 415, 2439

Rosales-Ortega, F. F., Sánchez, S. F., Iglesias-Páramo, J., et al. 2012, ApJL, 756, L31

Roskar, R., Debattista, V. P., Brooks, A. M., et al. 2010, MNRAS, 408, 783

Saintonge, A., Catinella, B., Tacconi, L. J., et al. 2017, ApJS, 233, 22

Sánchez Almeida, J., Elmegreen, B. G., Muñoz-Tuñón, C., & Elmegreen, D. M. 2014, A&ARv, 22, 71

Sánchez, S. F. 2020, ARA&A, 58, 99

Sánchez, S. F., Galbany, L., Pérez, E., et al. 2015, A&A, 573, A105

Sánchez, S. F., Rosales-Ortega, F. F., Iglesias-Páramo, J., et al. 2014, A&A, 563, A49

Sánchez, S. F., Rosales-Ortega, F. F., Marino, R. A., et al. 2012, A&A, 546, A2

Sánchez-Menguiano, L., Sánchez Almeida, J., Muñoz-Tuñón, C., et al. 2019, ApJ, 882, 9

Sánchez-Menguiano, L., Sánchez, S. F., Kawata, D., et al. 2016a, ApJL, 830, L40

Sánchez-Menguiano, L., Sánchez, S. F., Pérez, I., et al. 2016b, A&A, 587, A70

Sánchez-Menguiano, L., Sánchez, S. F., Pérez, I., et al. 2017, A&A, 603, A113

Sánchez-Menguiano, L., Sánchez, S. F., Pérez, I., et al. 2018, A&A, 609, A119

Schlafly, E. F., & Finkbeiner, D. P. 2011, ApJ, 737, 103

Schmidt, M. 1959, ApJ, 129, 243

Scholz-Diaz, L., Sánchez Almeida, J., & Dalla Vecchia, C. 2021, MNRAS, 505, 4655

Searle, L. 1971, ApJ, 168, 327

Sembach, K. R., & Savage, B. D. 1992, ApJS, 83, 147

Sembach, K. R., Tripp, T. M., Savage, B. D., & Richter, P. 2004, ApJS, 155, 351

Serra, P., Westmeier, T., Giese, N., et al. 2015, MNRAS, 448, 1922

Sharda, P., Wisnioski, E., Krumholz, M. R., & Federrath, C. 2021, MNRAS, 506, 1295

Skrutskie, M. F., Cutri, R. M., Stiening, R., et al. 2006, AJ, 131, 1163

Speagle, J. S., Steinhardt, C. L., Capak, P. L., & Silverman, J. D. 2014, ApJS, 214, 15

Springob, C. M., Haynes, M. P., Giovanelli, R., & Kent, B. R. 2005, ApJS, 160, 149

Stewart, K. R., Kaufmann, T., Bullock, J. S., et al. 2011, ApJ, 738, 39

Teklu, B. B., Gao, Y., Kong, X., Lin, Z., & Liang, Z. 2020, ApJ, 897, 61

Tinsley, B. M. 1973, ApJ, 186, 35

Tinsley, B. M. 1980, FCPh, 5, 287

Tinsley, B. M., & Larson, R. B. 1978, ApJ, 221, 554

Tortora, C., Hunt, L. K., & Ginolfi, M. 2022, A&A, 657, A19

Tremonti, C. A., Heckman, T. M., Kauffmann, G., et al. 2004, ApJ, 613, 898

Tumlinson, J., Thom, C., Werk, J. K., et al. 2013, ApJ, 777, 59

Vila-Costas, M. B., & Edmunds, M. G. 1992, MNRAS, 259, 121

Vincenzo, F., Belfiore, F., Maiolino, R., Matteucci, F., & Ventura, P. 2016a, MNRAS, 458, 3466

Vincenzo, F., Matteucci, F., Belfiore, F., & Maiolino, R. 2016b, MNRAS, 455, 4183

Wang, E., & Lilly, S. J. 2022, ApJ, 929, 95

Wang, J., Heckman, T. M., & Lehnert, M. D. 1997, ApJ, 491, 114

Weinberg, D. H., Griffith, E. J., Johnson, J. W., & Thompson, T. A. 2024, ApJ, 973, 15

Westmeier, T., Kitaeff, S., Pallot, D., et al. 2021, SoFiA 2: An Automated, Parallel HI Source Finding Pipeline, Astrophysics Source Code Library, ascl:2109.005

Xu, X., Heckman, T., Henry, A., et al. 2022, ApJ, 933, 222

Yin, S. Y., Liang, Y. C., Hammer, F., et al. 2007, A&A, 462, 535

Zaritsky, D., Kennicutt, R. C. J., & Huchra, J. P. 1994, ApJ, 420, 87